

# Testing *WMAP* data via *Planck* radio and SZ catalogues

J. R. Whitbourn,<sup>1</sup>\* T. Shanks<sup>1</sup> and U. Sawangwit<sup>1,2</sup>

<sup>1</sup>*Department of Physics, Durham University, South Road, Durham DH1 3LE, UK*

<sup>2</sup>*National Astronomical Research Institute of Thailand, 50200, Thailand*

Accepted 2013 October 6. Received 2013 October 4; in original form 2012 November 30

## ABSTRACT

The prime evidence underpinning the standard  $\Lambda$  cold dark matter cosmological model is the cosmic microwave background (CMB) power spectrum as observed by *Wilkinson Microwave Anisotropy Probe* (*WMAP*) and other microwave experiments. But Sawangwit and Shanks have recently shown that the *WMAP* CMB power spectrum is highly sensitive to the beam profile of the *WMAP* telescope. Here, we use the source catalogue from the *Planck* early data release to test further the *WMAP* beam profiles. We confirm that stacked beam profiles at  $Q$ ,  $V$  and particularly at  $W$ , appear wider than expected when compared to the Jupiter beam, normalized either directly to the radio source profiles or using *Planck* fluxes. The same result is also found based on *WMAP*-CMB-free source catalogues and NRAO VLA Sky Survey (NVSS) sources. The accuracy of our beam profile measurements is supported by analysis of CMB sky simulations. However, the beam profiles from *WMAP7* at the  $W$  band are narrower than previously found in *WMAP5* data and the rejection of the *WMAP* beam is now only at the  $\approx 3\sigma$  level. We also find that the *WMAP* source fluxes demonstrate possible non-linearity with *Planck* fluxes. But including ground-based and *Planck* data for the bright Weiland et al. sources may suggest that the discrepancy is a linear offset rather than a non-linearity. Additionally, we find that the stacked Sunyaev–Zel’dovich (SZ) decrements of  $\approx 151$  galaxy clusters observed by *Planck* are in agreement with the *WMAP* data. We find that there is no evidence for a *WMAP* SZ deficit as has previously been reported. In the particular case of Coma, we find evidence for the presence of an  $\mathcal{O}(0.1$  mK) downwards CMB fluctuation. We conclude that beam profile systematics can have significant effects on both the amplitude and position of the acoustic peaks, with potentially important implications for cosmology parameter fitting.

**Key words:** cosmic background radiation – large-scale structure of Universe.

## 1 INTRODUCTION

Cosmic microwave background (CMB) experiments such as the *Wilkinson Microwave Anisotropy Probe* (*WMAP*) have made significant progress in the study of the primordial temperature fluctuations. Their best-fitting power spectra strongly support a spatially flat,  $\Lambda$  cold dark matter ( $\Lambda$ CDM), universe. This model requires relatively few parameters, yet apparently manages a compelling concordance between a variety of other cosmological data; SNIa, large-scale structure and big bang nucleosynthesis. Although the statistical errors on these power spectra are small, this precision does not necessarily imply accuracy and there remains the potential for systematic errors to alter these conclusions.

Indeed, several anomalies between  $\Lambda$ CDM and the *WMAP* data have been discussed. Typically these have involved the large-scale

temperature multipoles, e.g. Bennett et al. (2011); Liu & Li (2011). However, other anomalies in the CMB at smaller scales have also been detected, connected in particular with radio sources (Sawangwit & Shanks 2010a,b) and Sunyaev–Zel’dovich (SZ) decrements from galaxy clusters (Myers et al. 2004; Bielby & Shanks 2007).

Radio sources are sometimes regarded as a contaminant in CMB temperature maps. However, radio point sources prove particularly interesting because they provide a complementary check of the beam measured by the *WMAP* team from observations of Jupiter (Page et al. 2003; Hill et al. 2009). Jupiter has a flux of  $\approx 1200$  Jy which is approximately three orders of magnitude higher than radio source fluxes or CMB fluctuations. This high flux has advantages in terms of defining the wings of the beam profile but has the disadvantage that the calibrating source is much brighter than typical CMB fluctuations. Furthermore, Jupiter only checks the beam on the ecliptic whereas radio sources are spread over the sky. Sawangwit & Shanks (2010a,b) made a stacked analysis of radio point sources and found evidence for a wider beam than *WMAP*

\* E-mail: joseph.whitbourn@durham.ac.uk

measured using Jupiter. A tentative detection of a non-linear relation between *WMAP* fluxes and ground-based radio telescope fluxes was also found. A thorough analysis of possible systematics did not find an explanation and we return to these issues later in this paper. The beam profile of a CMB telescope like *WMAP* is critical because it smoothes the temperature anisotropies and therefore needs to be known accurately to produce the final power spectrum from temperature maps (Page et al. 2003; Hill et al. 2009).

Various authors have noted small-scale anomalies with respect to the SZ decrements measured by *WMAP*. SZ decrements are created when CMB photons inverse Compton scatter off hot electrons in galaxy clusters. Myers et al. (2004) first stacked *WMAP* data at the positions of galaxy clusters and suggested that the profiles were more extended than expected. Lieu, Mittaz & Zhang (2006) and Bielby & Shanks (2007) then found that the SZ decrements from *WMAP* were reduced compared to X-ray predictions, possibly due to the *WMAP* beam being wider than expected. Bielby & Shanks (2007) also found that the *WMAP* decrements were significantly lower than the ground-based SZ measurements by Bonamente et al. (2006) in 38 X-ray luminous clusters.

In their early SZ (ESZ) sample, the *Planck* team find excellent agreement with the self-similar X-ray estimates of the SZ decrement (Planck Collaboration 2011e,d). This is corroborated by the ground-based South Pole Telescope Collaboration with their blind SZ-selected cluster sample (Mroczkowski et al. 2009). This compounds the question of why *WMAP* SZ analyses from Lieu et al. (2006) and Bielby & Shanks (2007) failed to find such an agreement.

In this paper, we use the recent *Planck* early data release and other radio source data to re-investigate both the *WMAP* radio source beam profile and SZ anomalies. The *Planck* Early Release Compact Source catalogue (ERCSC) is of particular interest and provides the basic parameters of radio sources and SZ clusters from the *Planck* CMB maps. Although the corresponding temperature maps from which these were estimated have not been released, both radio source fluxes and SZ profile parameters are available as measured by *Planck*. We can therefore use these to compare *WMAP* and *Planck* radio source fluxes directly and also to make *WMAP* stacks centred now on the new radio source and SZ cluster lists from *Planck*. From these stacks, the *WMAP* beam profile can be inferred and the SZ results from *WMAP* and *Planck* compared. Given the higher angular resolution, lower noise and different calibration strategy for *Planck*, this comparison will allow new insight into the robustness of the *WMAP* CMB analysis.

## 2 DATA

### 2.1 *Planck* early data release

The *Planck* team have recently made their first release of data collected by the *Planck* satellite between 2009 August 13 and 2010 June 6 (amounting to  $\approx 1.5$  full sky surveys). This early data release is concerned solely with the foreground contamination in the CMB maps. The two sets of catalogues relevant to this paper form the ERCSC. These are the radio source catalogues and the SZ catalogue.

#### 2.1.1 *Planck* radio sources

The ERCSC lists all the high-reliability radio sources with accurate flux determinations. The ERCSC has been quality controlled so that  $\geq 90$  per cent of the reported sources are reliable,  $> 5\sigma$ , detections

**Table 1.** Summary of the *Planck* bandpass parameters and the flux range of the sample we use from the ERCSC (Planck Collaboration 2011b).

Freq (GHz)	FWHM (arcmin)	Flux limit (Jy)
100	9.94	0.344
70	13.01	0.481
44	27.00	0.781

and that the fluxes are determined within  $\leq 30$  per cent accuracy. The catalogues are band specific and for the bands of interest ( $\nu \leq 100$  GHz) are created using the ‘PowellSnakes’ method, a Bayesian multifrequency algorithm for detecting discrete objects in a random background. Flux estimates were obtained by use of aperture photometry within a circle of the beam’s full width at half-maximum (FWHM). For the case of unresolved and potentially faint point sources, the *Planck* team recommend the use of the parameter FLUX and its corresponding error, FLUX\_ERR (Planck Collaboration 2011b).

We reject any extended objects from the catalogue to maintain an unresolved sample with which to test the *WMAP* data. To do this, we have used the *Planck* quality tag ‘EXTENDED’. This is defined by comparing the source areal profile with the 2D *Planck* beam. An additional quality flag ‘CMBSUBTRACT’ has also been provided, which reflects on the quality of the source detection in a map with the best estimate of the CMB removed. We minimize CMB contamination by using only CMBSUBTRACT = 0 sources.

When measuring the beam profile in Section 6, we further cut the catalogue to ensure the best quality sample. Sawangwit & Shanks (2010a) did suggest that their faintest *WMAP* source samples were probably affected by Eddington (1913) bias. To ensure the robustness of our results against Eddington bias, we have used an  $S \geq 1.1$  Jy flux cut, the same limit as previously used by Sawangwit & Shanks (2010a). We have additionally rejected sources within  $4^\circ$  of the Large Magellanic Cloud, sources at low galactic latitude,  $|b| < 5^\circ$  and any sources flagged by *Planck* as having high astrometric error. Finally, we tightened the *Planck* ‘EXTENDED’ flag to remove any sources intrinsically wider than the *WMAP* beam. The *Planck* ‘EXTENDED’ flag excludes sources with  $(\text{GAU}_{\text{FWHM\_MAJ}} \times \text{GAU}_{\text{FWHM\_MIN}})^{1/2} > 1.5 \times (\text{BEAM}_{\text{FWHM\_MAJ}} \times \text{BEAM}_{\text{FWHM\_MIN}})^{1/2}$ . We now ensure that the *Planck* sources are unresolved in the *WMAP* maps by imposing cuts in both the major and minor axis so that both the fitted Gaussian profiles (GAU) and the local point spread function (PSF) (BEAM) FWHM estimates are less than the FWHM of the *WMAP* beam in the band being studied.<sup>1</sup>

Band and colour corrections for the *WMAP* and *Planck* fluxes have been ignored. This factor is in any case small due to the typically flat spectral indices considered (Wright et al. 2009; Planck Collaboration 2011b). The full details of the catalogue construction and composition are described by Planck Collaboration (2011a) and briefly overviewed in Table 1.

<sup>1</sup> We relax this cut for the *Q* band, here we only impose cuts on local PSF (BEAM) FWHM estimates to ensure we get a reasonable number of sources.

### 2.1.2 Planck SZ catalogue

The ESZ catalogue lists all the robust and extensively verified SZ detections in the first data release. As described by Melin, Bartlett & Delabrouille (2006), the *Planck* team extract the integrated SZ signal, the  $Y$  parameter, using a Multifrequency Matched filter (MMF3) method (Planck Collaboration 2011a). The algorithm is run blindly on all-sky maps, assuming the characteristic SZ spectral signature and self-similar cluster profile.

In the early release of the *Planck* SZ catalogue, only data from the 100 GHz frequency channel or higher has been used to study the SZ effect. This is to avoid the detrimental effect on S/N from beam dilution caused by the larger beam sizes of the lower frequency channels. At the higher frequencies, the *Planck* beam FWHM is typically  $\approx 4.5$  arcmin. The full details of the catalogue construction and composition are described by the Planck Collaboration (2011a).

The catalogue provides estimates of the SZ flux, extent, redshift and position. It consists of 189 clusters, all detected at high S/N ( $\geq 6$ ) with 95 per cent reliability. Whilst the sample is primarily composed of known clusters (169/189), it provides a wealth of new information as it gives the first SZ measurements for  $\approx 80$  per cent of the clusters. In this paper, we only make use of clusters which have been pre-detected in the X-ray and have redshifts. We therefore, after masking, consider 151 clusters, including Coma. For this sample, the redshift range spans  $z \in [0.0126, 0.546]$  with a mean redshift of  $\bar{z} = 0.18$ .

### 2.2 WMAP data

We will be using the 7 yr *WMAP* temperature maps obtained from the LAMBDA CMB resource. We work with the  $N_{\text{side}} = 512$  HEALPIX maps resulting in a pixel scale of 7 arcmin. We use the foreground unsubtracted temperature band maps for  $Q$ ,  $V$  and  $W$ . Our default *WMAP* data sets are the co-added maps in  $Q$  ( $=Q1 + Q2$ ),  $V$  ( $=V1 + V2$ ) and  $W$  ( $=W1 + W2 + W3 + W4$ ). However, particularly in the  $W$  band, the increased S/N for radio source profiles obtained by using all the differencing assemblies (DA) can be regarded as a trade-off with the precision of just using the narrowest  $W1$  (and  $W4$ ) beams as previously used by Sawangwit & Shanks (2010a). In using the co-added data, the Jupiter beams have to be combined before comparison with the data. We estimate the Jupiter beam in each band by averaging the 7 yr beam profiles from the various detector assemblies, assuming the appropriate correction for pixelization (Hinshaw et al. 2003). When working with radio point sources, we use the point-source catalogue mask (`wmap_point_source_catalog_mask`). To avoid Galactic contamination for the SZ analyses, we have instead used the extended temperature mask (`wmap_ext_temperature_analysis_mask`) which admits 71 per cent of the sky.

We have used the 7 yr *WMAP* 5-band point-source catalogue (Gold et al. 2011). These sources are detected at least the  $5\sigma$  level in one *WMAP* band. For a flux density to be stated, the detection must be above the  $2\sigma$  level in that band. Following Sawangwit & Shanks (2010a), we ensure that the sources are genuinely point sources by matching to the 5 GHz ( $\approx 4.6$  arcmin resolution) catalogues from the Greenbank Northern sky Survey (GB6; Gregory et al. 1996), or Parkes-MIT-NRAO (PMN; Griffith & Wright 1993) surveys. The *WMAP* team also provide a 7 yr CMB-free catalogue as described by Gold et al. (2011). This catalogue has been created with the objective of detecting point sources free of boosting by CMB fluctuations. We proceed with the raw 5-band catalogue with 471 sources and a CMB-free catalogue with 417 sources.

## 3 PLANCK RADIO SOURCE FLUXES AND SZ CLUSTER DECREMENTS

### 3.1 Conversion of radio flux to temperature profiles

The *Planck* ERCSC provides us with the source flux density, error and a few parameters on the source characteristics and detection. To enable us to translate the *Planck* fluxes into *WMAP* observables, we need to convert the source flux density,  $S_{\text{tot}}$ , into an observed peak Rayleigh–Jeans antenna temperature using the conversion factor  $\Gamma^{\text{ff}}(\nu)$  (Page et al. 2003),

$$\Delta T_{\text{RJ}}(0) = S_{\text{tot}} \Gamma^{\text{ff}}(\nu), \quad (1)$$

where

$$\Gamma^{\text{ff}}(\nu) = \frac{c^2}{2k_{\text{b}} \nu_{\text{e}}^2} \frac{1}{\Omega_{\text{beam}}(\nu)}. \quad (2)$$

Here  $\nu_{\text{e}}$  is the effective frequency of the bandpass and the ff superscript denotes the fact that the majority of the *WMAP* sources have a spectral index  $\alpha \approx -0.1$ , approximately that of free–free emission.

The *WMAP* temperature maps are given in terms of the thermodynamic temperature. At the *WMAP* frequencies and CMB temperature, the Rayleigh–Jeans temperature is appreciably different from this. We therefore correct between the two temperature differences, using equation (3), where  $x' = h\nu/k_{\text{b}}T_{\text{cmb}}$  and  $T_{\text{cmb}} = 2.725$  K is the monopole temperature of the CMB (Jarosik et al. 2003).

$$\begin{aligned} \Delta T_i &= \frac{(e^{x'} - 1)^2}{x'^2 e^{x'}} \Delta T_{\text{RJ}}, \\ &= g(\nu) \Delta T_{\text{RJ}}. \end{aligned} \quad (3)$$

The observed *WMAP* temperature profiles therefore take the form,

$$\begin{aligned} \Delta T(\theta) &= \Delta T(0) b^s(\theta), \\ &= g(\nu) \Gamma^{\text{ff}} S_{\text{tot}} b^s(\theta). \end{aligned} \quad (4)$$

We see the beam dependence of the observed profile is twofold. The shape is dependent on the symmetrized beam profile  $b^s(\theta)$  (normalized to unity at  $\theta = 0^\circ$ ), while the scale is normalized by the beam solid angle associated with  $\Gamma^{\text{ff}}$ . A summary of the assumed values of  $g(\nu)$  and  $\Gamma^{\text{ff}}$  is provided in Table 2.

### 3.2 Planck SZ decrements

*Planck* presents its observed decrements using an SZ model fit parametrized by the total SZ signal within the cluster extent. Here, we briefly describe this model so that the *Planck* results can be compared to the stacked *WMAP* temperature decrements.

Clusters are significant reservoirs of gas which will result in a SZ distortion to the CMB described by the Compton  $y$  parameter,

$$\Delta T(\theta) = T_{\text{cmb}} j(x') y(\theta). \quad (5)$$

**Table 2.** Summary of the *WMAP* bandpass parameters taken from Hill et al. (2009) and Jarosik et al. (2011) – see the text for definitions.

Band	Freq (GHz)	FWHM (arcmin)	$\Omega$ (sr)	$\Gamma^{\text{ff}}$ ( $\mu\text{KJy}^{-1}$ )	$g(\nu)$
$W$	94	12.6	$2.097 \times 10^{-5}$	179.3	1.245
$V$	61	19.8	$4.202 \times 10^{-5}$	208.6	1.099
$Q$	41	29.4	$8.978 \times 10^{-5}$	216.6	1.044

**Table 3.** Summary of the *Planck* NFW parameters as used in equation (10) and described by Arnaud et al. (2010). These are the same parameters as used by the *Planck* team, the All:Fitted set.

Type	$P_0$	$c_{500}$	$\gamma$	$\alpha$	$\beta$
All:Fitted	$8.403 \left(\frac{h}{0.7}\right)^{-\frac{3}{2}}$	1.177	0.3081	1.0510	5.4905

Here,  $j(x')$  is the spectral function, where  $x' = h\nu/k_b T_{\text{cmb}}$  (Sunyaev & Zeldovich 1980),

$$j(x') = \frac{x'(e^{x'} + 1)}{e^{x'} - 1} - 4. \quad (6)$$

The integrated  $Y$  parameter is the total SZ signal, which is simply the integration of the Compton  $y$  parameter on the sky,

$$Y = \int y d\Omega. \quad (7)$$

Alternatively, if we integrate over the cluster volume,

$$Y = \frac{\sigma_t}{m_e c^2} \int P dV. \quad (8)$$

However, we are observing a 2D projection of the cluster<sup>2</sup> on the sky. The angle  $\theta$  we observe on the sky, corresponds in 3D to a cylindrical bore through the cluster of radius  $R = \theta D_a(z)$ , where  $D_a$  is the angular diameter distance. The observed integrated  $Y$  parameter therefore takes the form Arnaud et al. (2010),

$$\begin{aligned} Y_{\text{cyl}}(R) &= \frac{\sigma_t}{m_e c^2} \int_0^R 2\pi r dr \int_r^{R_{\text{tot}}} \frac{2P(r')r' dr'}{(r'^2 - r^2)^{1/2}}, \\ &= Y_{\text{sph}}(R_{\text{tot}}) - \frac{\sigma_t}{m_e c^2} \int_R^{R_{\text{tot}}} 4\pi P(r)(r^2 - R^2)^{1/2} r dr. \end{aligned} \quad (9)$$

To predict the SZ effect implied by equation (9), we have to make a choice of the pressure profile,  $P(r)$ . Historically, it has been common to fit the SZ profile with an isothermal  $\beta$  model (Cavaliere & Fusco-Femiano 1976). However, X-ray observations have shown that the assumption of an isothermal gas breaks down at the cluster outskirts (Piffaretti et al. 2005; Pratt et al. 2007). To account for this additional complexity Nagai, Vikhlinin & Kravtsov (2007) proposed using a Generalized Navarro Frenk White (GNFW) profile for the pressure instead. The profile is scale invariant in that it is independent of absolute distances and is instead a function of the dimensionless scale  $x = R/R_{500}$ . The profile takes the form,

$$\mathcal{P}(x) = \frac{P_0}{(c_{500}x)^\gamma [1 + (c_{500}x)^\alpha]^{(\beta-\gamma)/\alpha}}, \quad (10)$$

where  $\mathcal{P}(x) = P(r)/P_{500}$  and  $P_{500}$  is the characteristic pressure defined by Arnaud et al. (2010).

Here, we have a five-parameter fit to the pressure profile ( $P_0$ ,  $c_{500}$ ,  $\gamma$ ,  $\alpha$  and  $\beta$ ). This allows independent specification of the pressure in the cluster core ( $\gamma$ ), main body ( $\alpha$ ) and outskirts ( $\beta$ ). In Table 3, we outline the parameters used by *Planck*, as taken from Arnaud et al. (2010). The characteristic parameters of the cluster are  $M_{500}$ ,  $P_{500}$  and  $R_{500}$  (see Appendix A), where the 500 denotes the fact that they are evaluated within the region where the mean mass density is 500 times greater than the critical density  $\rho_{\text{crit}}(z)$ . The *Planck* team extract the integrated  $Y$  parameter using the MMF3 method (Planck Collaboration 2011a) based on the above self-similar model. The integration is done to the angular cluster

extent corresponding to  $5R_{500}$ , which *Planck* also report ( $\theta_{5R_{500}}$ ). Their errors on the integrated SZ signal,  $Y$ , combine their estimated measurement error with Monte Carlo estimates of the error due to uncertainties within the self-similar model (Melin et al. 2006).

### 3.3 SZ temperature profile reconstruction

We now proceed to invert the *Planck* data to provide us with expected *WMAP* temperature profiles – see Appendix A for the details of this derivation. From the *Planck* values for  $Y(5R_{500})$  and  $\theta_{5R_{500}}$ , and using  $J(x)$  and  $I(x)$ , the cylindrical and spherical SZ templates (see equation (A7)) we first obtain  $Y_{\text{cyl}}(R)$  via equation (A9),

$$Y_{\text{cyl}}(R) = Y_{\text{cyl}}(5R_{500}) \left(1 - \frac{J(x)}{I(5)}\right). \quad (11)$$

From this integrated  $Y_{\text{cyl}}(R = \theta \cdot D_a(z))$ , we want to derive the angular dependence of the Compton  $y$  parameter, where  $y(\theta) = \frac{d}{d\Omega} Y_{\text{cyl}}(\theta)$ , and so

$$y(\theta) = -\frac{Y_{\text{cyl}}(5R_{500})}{I(5)} \frac{d}{d\Omega} (J(x)). \quad (12)$$

The self-similar model therefore predicts an SZ temperature decrement,

$$\Delta T_{\text{SZ}}(\theta) = -T_{\text{cmb}} j(x') \frac{Y_{\text{cyl}}(5R_{500})}{I(5)} \frac{d}{d\Omega} (J(x)), \quad (13)$$

where  $Y_{\text{cyl}}(5R_{500})$  is the integrated  $Y$  given in the ESZ.

### 3.4 Convolution with the WMAP beam profile

The cluster profile is not directly observed by *WMAP* and is instead smoothed by the instrument response. The predicted *WMAP* SZ profile therefore results from the 2D convolution of equation (13) with the *WMAP* beam profile. Myers et al. (2004) and Bielby & Shanks (2007) assumed that the source is well resolved with respect to the *WMAP* beam. Under this assumption the full form for a 2D convolution can be approximated by a 1D convolution.<sup>3</sup> However, the typical cluster sizes used in SZ studies are of the same order as the *WMAP* beams and so this approximation can start to fail. Furthermore, for profiles such as the self-similar model which are very centrally peaked this approximation becomes increasingly invalid. The implementation of the PSF convolution used in this paper is fully 2D and does not rely on such approximations. In Section 9.4, we explore the impact of this on the Bielby & Shanks (2007) results.

## 4 CROSS-CORRELATION METHODS

### 4.1 Stacking positions

The choice of coordinates to use for the radio source positions and cluster centres is important. Scatter or an offset in the centroid used in the cross-correlation could cause the stacked result to appear artificially broad or induce artefacts. However, the only sample used in this paper for which astrometric errors are appreciable are the

<sup>3</sup> Taking a Gaussian beam as an example, if  $\sigma_{\text{beam}}$  is much smaller than the typical scale of the cluster profile then the  $\theta$  integral in Bailey & Sparks (1983)'s equation (2) which describes the non-radial aspect (i.e. the 2D nature) of the convolution is approximately  $2\pi$ . This effectively reduces the dimensionality of the convolution, which now takes a 1D Gaussian form.

<sup>2</sup> The cluster is assumed to be spherical.

*WMAP* derived radio-source catalogues where the astrometric error in both longitude and latitude is 4 arcmin (Chen & Wright 2009). We mitigate for this effect by using the position of the corresponding matched 5GHz source, since these have negligible astrometric error  $\mathcal{O}(10)$  arcsec (Griffith & Wright 1993; Gregory et al. 1996). We find no evidence for an offset between the *WMAP* and 5 GHz sources and hence we are confident that astrometry error will not cause new broadening of the beam. We also note that the stacking procedure we use is dominated by the brighter objects, which typically have better astrometry.

For the *Planck* radio source catalogues, we have used the *Planck* positions since these are of high astrometric quality (Planck Collaboration 2011b). In our sample selection, we have rejected sources which the *Planck* team estimate to have relatively high astrometric errors. The effect of this selection in the 100 GHz band is to ensure that  $\sigma < 0.75$  arcmin for the  $S \geq 1.1$  Jy sample.

For the *Planck* SZ objects, we have taken the *Planck* estimated positions rather than the X-ray derived positions as the cluster centres. We do this to avoid the complications associated with rare but potentially large offsets between the SZ and X-ray signals which are likely caused by merging events (Planck Collaboration 2011a).

## 4.2 Calculation of profiles

Our cross-correlation/stacking procedures for measuring both radio point-source profiles and SZ decrements are similar to those of Myers et al. (2004), Bielby & Shanks (2007) and then as updated by Sawangwit & Shanks (2010a). Ultimately, we shall be stacking/cross-correlating *WMAP* data around radio source positions and cluster centres from catalogues, particularly from the *Planck* ERCSC. To estimate a temperature profile for an individual source  $j$  we use,

$$\Delta T_j(\theta) = \sum_i \frac{T_{ij}(\theta) - \bar{T}_j}{n_{ij}(\theta)}, \quad (14)$$

where the sum is over the pixels, denoted  $i$ , within a circular annulus of radius  $\theta$ . Here  $n_{ij}$  represents the number of pixels within the annulus and  $T_{ij}$  is the temperature recorded for the pixel  $i$  and source  $j$ .  $\bar{T}_j$  is the average background temperature which can either be estimated locally in a surrounding annulus in a ‘photometric method’ or globally – see Sawangwit & Shanks (2010a). These two background estimates make no difference in the stacked results but can make a difference for individual sources – see Section 9. We then stack the *WMAP* data by averaging  $\Delta T_j(\theta)$  over the sources that have pixels within the annulus  $\theta$  using the statistical average,  $\Delta T(\theta) = \sum_j (1/N_\theta) \Delta T_j(\theta)$ .  $N_\theta$  is the number of sources that have pixels within the annulus  $\theta$  and is usually constant for all except the  $\theta \lesssim 4$  arcmin bins.

We have followed Sawangwit & Shanks (2010a) in using jack-knife errors, for both the radio and SZ sources, based on six equal area sub-fields defined by lines of constant galactic longitude and split by the galactic equator. For  $N = 6$  fields denoted  $k$ , the errors are,

$$\sigma^2(\theta) = \frac{N-1}{N} \sum_k \left( \Delta T_k(\theta) - \overline{\Delta T}(\theta) \right)^2, \quad (15)$$

where  $\Delta T_k(\theta)$  is the average of the fields excluding field  $k$ . We have experimented with both alternative sub-fields and methods such as bootstrap re-sampling finding approximately equivalent results. In Section 7.1, we have used simulations to test whether our method

can robustly recover the beam profile, in doing so we find that our jack-knife errors are reasonable.

## 5 FLUX COMPARISONS

### 5.1 Gold et al. (2011) *WMAP*7 and *Planck* ERCSC

We first compare *WMAP*7 sources at  $Q$ ,  $V$ ,  $W$  from Gold et al. (2011) to their counterparts in the *Planck* ERCSC at 100, 70 and 44 GHz. We also compare the *Planck* fluxes in the 100 GHz band to the ground-based Australia Telescope Compact Array (ATCA; Sadler et al. 2008) and Institut de Radioastronomie Millimétrique (IRAM; Steppe et al. 1988) source fluxes previously used by Sawangwit & Shanks (2010a).

In Fig. 1, we first focus on the comparison of the *WMAP*7 fluxes to *Planck* and also the ground-based ATCA and IRAM sources.

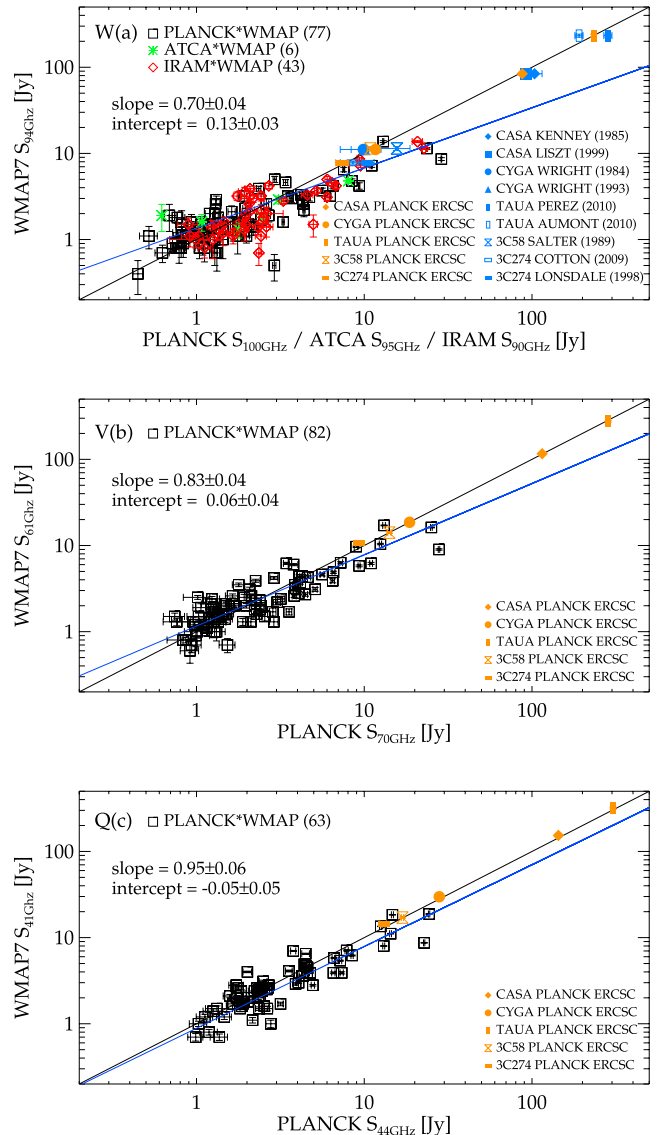


**Figure 1.** A comparison between the *WMAP*7 fluxes, *Planck* and ground-based source fluxes. Also shown are the one-to-one relation (black line) and the best-fitting relation (blue line). Measurements of the Weiland et al. (2011) sources have been corrected to a *WMAP* epoch of 2005 and the respective *WMAP* band centres using the Weiland et al. (2011) variability estimates and spectral indices.

We only consider the matches with separation less than 2 arcmin to avoid any possible systematic errors associated with sources that have poor astrometry. However, our results are independent of this cut up to separations of 10 arcmin. At high fluxes, we see evidence for a systematically lower *WMAP* flux,  $\approx 50$  per cent above 2 Jy. This non-linearity is particularly prominent in the *W* band, the band with the greatest angular resolution.

Since there are errors in both variables, we have used the Numerical Recipes (Press et al. 1992) *fitexy* as our fitting routine. We find best-fitting logarithmic slopes of  $[0.70 \pm 0.04, 0.83 \pm 0.04, 0.95 \pm 0.06]$  for the  $[100 \text{ GHz-}W, 70 \text{ GHz-V}, 44 \text{ GHz-Q}]$  comparisons. To obtain realistic errors on these fits, we have linearly scaled the flux errors until we obtained a  $\chi^2$  probability of 0.5 as recommended by Press et al. (1992), for data with a dominant intrinsic dispersion.

Clearly, *Planck* and *WMAP* fluxes for sources were measured at different times. Since at least  $\approx 30$  per cent of the *WMAP5* radio sources exhibit some level of variability (Wright et al. 2009), we expect and observe much larger scatter than accounted for by the estimated flux uncertainty. However, we note that the brighter *WMAP* sources are fainter than the one-to-one relation, this is in the opposite sense expected if variability was biasing faint *Planck* sources into the *WMAP* catalogue when in a bright phase.

We investigate whether variability is alternatively causing a bias due to *Planck* dropouts by limiting the *WMAP* sample to  $\geq 5\sigma$  sources. The advantage is that the *Planck* team have investigated all the *WMAP*  $\geq 5\sigma$  objects that are not in the ERCSC. They conclude that for the 100 GHz-*W* comparison the missing objects are ‘all’ spurious and can be explained by the object having a weak or missing 5 GHz ID (Planck Collaboration 2011b). The resulting  $\geq 5\sigma$  *WMAP* *W*-band sample of 48 sources (with  $S \geq 0.8$  Jy) is therefore complete in the sense of being 100 per cent represented in the *Planck* sample with no bias due to a *Planck* dropout population. When we then repeat the *WMAP-Planck* 100 GHz-*W* flux comparison, we find a logarithmic slope of  $(0.67 \pm 0.05)$ , consistent with the original result and therefore strong evidence against a highly variable source population causing dropouts that bias the *-Planck* comparison.

The disagreement between *Planck* and *WMAP* is in contrast to direct comparisons between *Planck* and ground-based ATCA/IRAM data. These instead show good agreement, as shown in Fig. 2 for the *Planck* 100 GHz radio point-sources. The best-fitting logarithmic slope of  $[0.95 \pm 0.05]$  is statistically consistent with the one-to-one relation. However, comparing *WMAP* *W*-band and the ground-based ATCA/IRAM data we find evidence for non-linearity with a best-fitting logarithmic slope of  $[0.72 \pm 0.04]$ . These contrasting fits are particularly significant because the greatest *Planck-WMAP* non-linearity comes from the 100 GHz-*W* flux comparison. Given the agreement between *Planck* and the ground-based ATCA/IRAM observations, we interpret the flux disagreement as being due to *WMAP*.

## 5.2 Further tests for bias

In response to the referee, we have made additional bootstrap and jack-knife re-sampling tests of the *WMAP\*Planck* flux-flux comparison and its error. After 1000 bootstrap re-samplings, we estimate logarithmic slopes of  $[0.70 \pm 0.09, 0.84 \pm 0.11, 0.95 \pm 0.10]$  for the  $[100 \text{ GHz-}W, 70 \text{ GHz-V}, 44 \text{ GHz-Q}]$  comparisons. We also perform jack-knife re-samplings of the *WMAP\*Planck* flux-flux comparison, we estimate a logarithmic slope of  $[0.70 \pm 0.10, 0.83 \pm 0.12, 0.95 \pm 0.10]$  for the  $[100 \text{ GHz-}W, 70 \text{ GHz-V}, 44 \text{ GHz-Q}]$  compar-

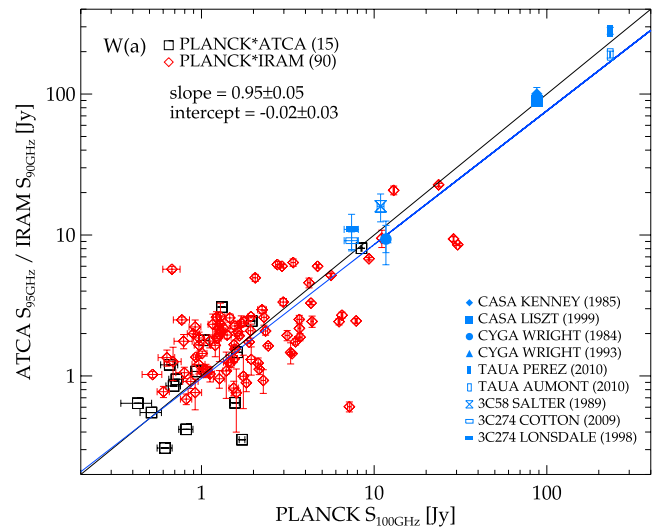


**Figure 2.** A comparison of the 100 GHz *Planck* fluxes and the ground-based sources. Also shown are the one-to-one relation (black line) and the best-fitting relation (blue line). Measurements of the Weiland et al. (2011) sources have been corrected to a *Planck* ERCSC epoch of 2010 and the respective *Planck* band centres using the Weiland et al. (2011) variability estimates and spectral indices.

isons. These re-sampling results are consistent with our original samples and support the accuracy of our previous error analysis.

We have also made Monte Carlo simulations of the flux-flux comparison. We generated samples with the same number of sources as in the real flux-flux comparison using the *WMAP* *Q*-band power-law distribution,  $N(< S) \propto S^{-1.7}$  (Bennett et al. 2003). These fluxes are then scaled to the respective *WMAP* and *Planck* band centres on the basis of a Gaussian distribution in spectral indices,  $\alpha$ , with mean  $-0.09$  and standard deviation  $0.176$  (Wright et al. 2009). Realistic Gaussian measurement errors are then assigned as a function of flux in a manner consistent with the original *WMAP* and *Planck* samples. To include variability, we start from the Wright et al. (2009) analysis of the *WMAP5* data that measured a median rms flux variability for the 25 brightest *Q*-band objects of  $\sigma = 0.23$  and which we therefore additionally apply to all our sources, assuming a Gaussian distribution. We then impose detection limits corresponding to the faintest source in the given band for the *WMAP* and *Planck* fluxes, respectively. Finally, we compare these two flux types by measuring the best-fitting relation in the same way as was originally done for the *Planck-WMAP* comparison. After 10 000 simulations of the 100 GHz-*W* comparison, we find average logarithmic slopes and intercepts of  $[0.98 \pm 0.06]$  and  $[0.04 \pm 0.06]$ . These results are not only in agreement with a one-to-one relation but support the errors found in our original *WMAP-Planck* comparison. We therefore conclude we are able to robustly recover the expected one-to-one result and hence that our comparison may be unbiased.

## 5.3 Potential contamination of *Planck* fluxes by CO emission

Planck Collaboration (2011b) have noted that the 100 GHz bandpass contains the  $J = 1 \rightarrow 0$  rotational CO emission line. This is a potential explanation for the flux non-linearity we report between the *WMAP* 94 GHz *W* band and *Planck* 100 GHz bands. However, such an explanation would imply that *WMAP* and *Planck* are in agreement away from the galactic plane where CO emission is lower. However, we see no evidence for such a distinction, with galactic latitude cuts of  $|b| > 5^\circ$ ,  $|b| > 30^\circ$  and  $|b| > 45^\circ$  we find

100 GHz-*W* logarithmic slopes of  $[0.70 \pm 0.04]$ ,  $[0.65 \pm 0.06]$  and  $[0.72 \pm 0.08]$ , respectively.

#### 5.4 Inclusion of the five additional Weiland et al. (2011) bright sources

Weiland et al. (2011) have made a comparison of *WMAP* fluxes of bright radio source fluxes from ground-based telescopes and claim that they support the *WMAP* flux scale. Some of the sources used are planets and have not been through the same reduction procedures as the CMB maps but five other sources, Cyg A, Cas A, Tau A, 3C58 and 3C274 have gone through the same procedures. Weiland et al. (2011) selected these sources on the basis that they were the brightest and least variable of the sources with adequate background contrast and a history of prior observation.

We now expand our flux comparisons by including these Weiland et al. (2011) sources in Fig. 1. We use the *WMAP* fluxes quoted by these authors and the independent ground-based fluxes that are mostly those quoted by these authors. We see that in the *W* band at least, *WMAP* also underestimates the flux of these sources (blue points) and indeed Cyg A, 3C274 and 3C58 appear not inconsistent with our fitted relation. However, the underestimation for Cas A is less than predicted by extrapolating the fit to the brighter radio fluxes. If this result were to be more highly weighted then there would still be evidence for a *WMAP* flux problem, but one which now looked more like a constant offset than a scale error. However, we note that there are differences between the two ground-based observations of Cas A. Furthermore, Cas A lies close to the galactic plane ( $|b| < 6^\circ$ ) and hence contamination might be an issue. We also note that for the brightest source, Tau-A, *WMAP* in fact overestimates the Aumont et al. (2010) measurement. However, there is a considerable difference between the Weiland et al. (2011) and Macías-Pérez et al. (2010) estimates of the *WMAP* flux. This is again likely due to the difficulty of background subtraction for a source in the galactic plane ( $|b| < 6^\circ$ ). It may therefore be too early to infer a flux offset on the basis of these sources.

When we include the Celestial sources from Weiland et al. (2011) with independent ground-based measurements<sup>4</sup> into the *Planck*–*WMAP* comparison, we find a logarithmic slope of  $0.87 \pm 0.04$  for the 100 GHz-*W* comparisons. After jack-knife and bootstrap re-sampling, we find logarithmic slopes of  $0.87 \pm 0.09$  and  $0.86 \pm 0.08$ , respectively, for the 100 GHz-*W* comparisons. Hence, whilst including the Celestial source data changes the degree of the non-linearity, the results are still in significant disagreement with a one-to-one relation.

We finally add the *Planck* ERCSC measurements of these five sources to Figs 1 and 2. This complicates the picture further since they appear to agree with the *WMAP* results more than the ground-based results. As far as we can see, the *Planck* fluxes are not calibrated via *WMAP*. If we then fit the full *Planck*–*WMAP* *W*-band comparison, we now find less evidence for a discrepancy between the two finding a 100 GHz-*W* logarithmic slope of  $[0.91 \pm 0.04]$ . But just making the 100 GHz-*W* comparison in the 3–400 Jy region, the result might then again look more like a constant offset with a logarithmic slope and intercept of  $[1.01 \pm 0.10]$  and  $[0.16 \pm 0.12]$ .

We conclude that the *WMAP* fluxes in the  $S \approx 10$  Jy region show systematically lower fluxes than *Planck* and we have argued that

this discrepancy is unlikely to be explained by variability, underestimated errors or inaccurate flux estimation. At lower and higher fluxes, the *WMAP*–*Planck* agreement seems better, implying some non-linearity in their relative scales. If *WMAP* data are compared to ground-based data rather than *Planck*, the same discrepancy is seen at  $S \approx 10$  Jy and a small but significant discrepancy is seen at brighter fluxes, which would more imply a linear offset rather than a non-linearity. Similar effects are seen at *Q* and *V* but at a lower level.

## 6 *WMAP* POINT-SOURCE PROFILES

### 6.1 *Planck* ERCSC radio sources

We now apply the stacking analysis of Sawangwit & Shanks (2010a) to the co-added *WMAP7* maps, centring on the *Planck* radio point-sources. *Planck* sources are selected at multiple wavebands which may be advantageous in avoiding spurious sources etc. Figs 3(a), (b) and (c) are shown for completeness because these raw temperature plots demonstrate the main uncertainty in this analysis which is the accuracy of the background subtraction. We note that there is some difference between the global background and the background local to the source samples but generally this effect appears smaller in the *WMAP7* data (e.g. at *W*) than it was in the *WMAP5* data sets used by Sawangwit & Shanks (2010a).

Figs 3(d), (e) and (f) show the same profiles now background subtracted and scaled to unity at the origin to produce  $b^S(\theta)$ . We have used the ‘photometric’ subtraction to produce the radio point-source temperature profile,  $\Delta T_{\text{radio}}(\theta)$ . For the *WMAP7* data set, there is very little difference in the profiles resulting from global or local/photometric background subtractions.

These  $b^S(\theta)$  are now compared to the *WMAP* Jupiter beam and the best-fitting beam to the bright *WMAP* radio source profiles found by Sawangwit & Shanks (2010a) (dashed orange line in their fig. 2). There is again evidence that the *Planck*-selected radio sources suggest a wider beam than the Jupiter beam, particularly in the *W* band, although the *Planck* sources lie slightly below the profile fits from Sawangwit & Shanks (2010a). We further note that the statistical significance of the deviations from the Jupiter beam for the *Planck*-selected sources at 12.6–19.9 arcmin is only modest at  $\approx 2\text{--}3\sigma$  for the *W* band.

The normalization of  $b^S(\theta)$  to unity at small scales forms a further uncertainty in these beam comparisons. In Figs 3(g), (h) and (i), we have applied the formalism of Section 3.1 and attempted to make absolute normalizations of the various model profiles, using the *Planck* ERCSC listed fluxes. We assume in turn the Jupiter profile and then the radio source profile of Sawangwit & Shanks (2010a) in calculating the resulting  $\Gamma^{\text{ff}}$  factor. These give respectively the blue and red lines. Hence, if the radio sources followed the Jupiter profile, for example, we should see the same peak temperature for the stacked model profile and the stacked data. We see that the *Planck* peak temperatures, particularly in the *W* band, tend to lie between the Jupiter profile and the previous *WMAP* bright radio source fits. These results suggest that the previous radio source fit may be too wide at  $\theta > 30$  arcmin where it is essentially an extrapolation, unconstrained by the data, and this will affect the accuracy of its absolute normalization i.e. there is a large error in  $\Omega_{\text{beam}}$ . Otherwise, the conclusion is similar to that from Figs 3(d), (e) and (f) in that the *Planck* data is suggesting that the Jupiter beam is a poor fit to the radio source profiles particularly at *W*.

The question of Eddington bias was discussed by Sawangwit & Shanks (2010a) and has also been suggested by Schultz &

<sup>4</sup> We do not include measurements without error estimates, this excludes the Cyg A Wright & Sault (1993) and 3C274 Lonsdale, Doeleman & Phillips (1998) measurements.

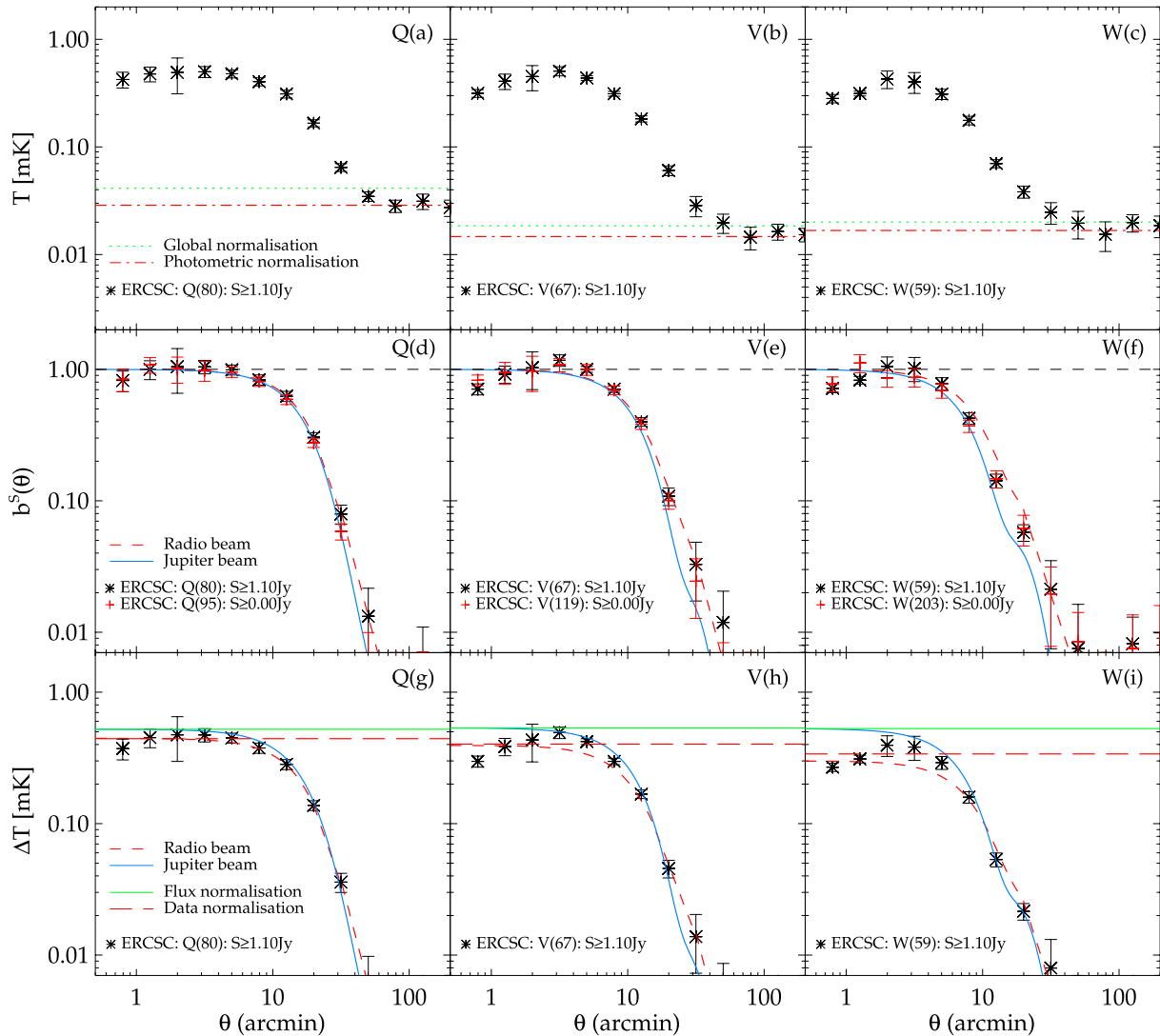


**Figure 3.** (a),(b),(c): the raw stacked *WMAP7* [*Q,V,W*] temperature profiles for the *Planck* [44,70,100] GHz band sources with the global mean and photometric background temperatures of the map plotted as dashed (green, red) lines. (d),(e),(f): the photometrically subtracted, stacked and re-normalized *WMAP7* [*Q,V,W*]  $b^S(\theta)$  profiles for the *Planck* [44,70,100] GHz band sources. Also shown are the  $b^S(\theta)$  for the Jupiter beam (blue, solid) and the radio source fit (red, dashed) of Sawangwit & Shanks (2010a). Any sensitivity to Eddington bias is shown in the profiles without the flux limit of  $S \geq 1.1$  Jy (lighter red, cross). (g),(h),(i): the photometrically subtracted and stacked *WMAP7* [*Q,V,W*]  $\Delta T(\theta)$  profiles for the *Planck* sources. Also shown are the  $\Delta T(\theta)$  for the Jupiter beam (blue, solid) and the radio source fit (red, dashed) of Sawangwit & Shanks (2010a), now absolutely normalized via the *Planck* flux.

Huffenberger (2011) as a possible explanation of the wide radio profiles. In terms of the *Planck* sources an Eddington bias of  $\approx 0.02$  mK is required to explain our results. However, our pre-selection of these sources as being point-like at *Planck* resolution and our rejection of both faint ( $S < 1.1$  Jy) and CMB-contaminated sources mean that it is difficult to see how Eddington bias could be affecting these results. In Figs 3 (d),(e),(f), we have also presented the source sample without the  $S \geq 1.1$  Jy flux cut. The consistency of the full source and brighter source samples indicates that Eddington bias is not significantly affecting these samples.

## 6.2 *WMAP7* radio sources

We next repeat the analysis of Sawangwit & Shanks (2010a) using the co-added *WMAP7* maps and source catalogue (Gold et al. 2011). The results are shown in Fig. 4. We see that the results again tend to lie between the Jupiter profile and the previous *WMAP* bright

radio source fits by Sawangwit & Shanks (2010a). This may in part be due to the *WMAP7* profiles returning to zero at large scales more uniformly than *WMAP5*, making the differences between the photometric and global profile estimates more marginal. However, we also found that using the *WMAP5/WMAP7* catalogue in the *WMAP7/WMAP5* temperature maps gives profiles more consistent with the Sawangwit & Shanks (2010a) fits. We therefore attribute the difference between Fig. 4 and the results of Sawangwit & Shanks (2010a) to a possible systematic difference between *WMAP5* and *WMAP7*, with perhaps a contribution from statistical fluctuations.

Following Sawangwit & Shanks (2010a), we minimized any effect of Eddington bias for this sample by pre-selecting only sources that appear in the 5 GHz GB6 and PMN radio samples. We have only used 5 GHz coordinates for the radio sources, with their sub-30 arcsec accuracy to minimize any positional error in our analysis. Although Eddington bias may well be affecting the faintest *WMAP* sources, as was also noted in Sawangwit & Shanks (2010a), we

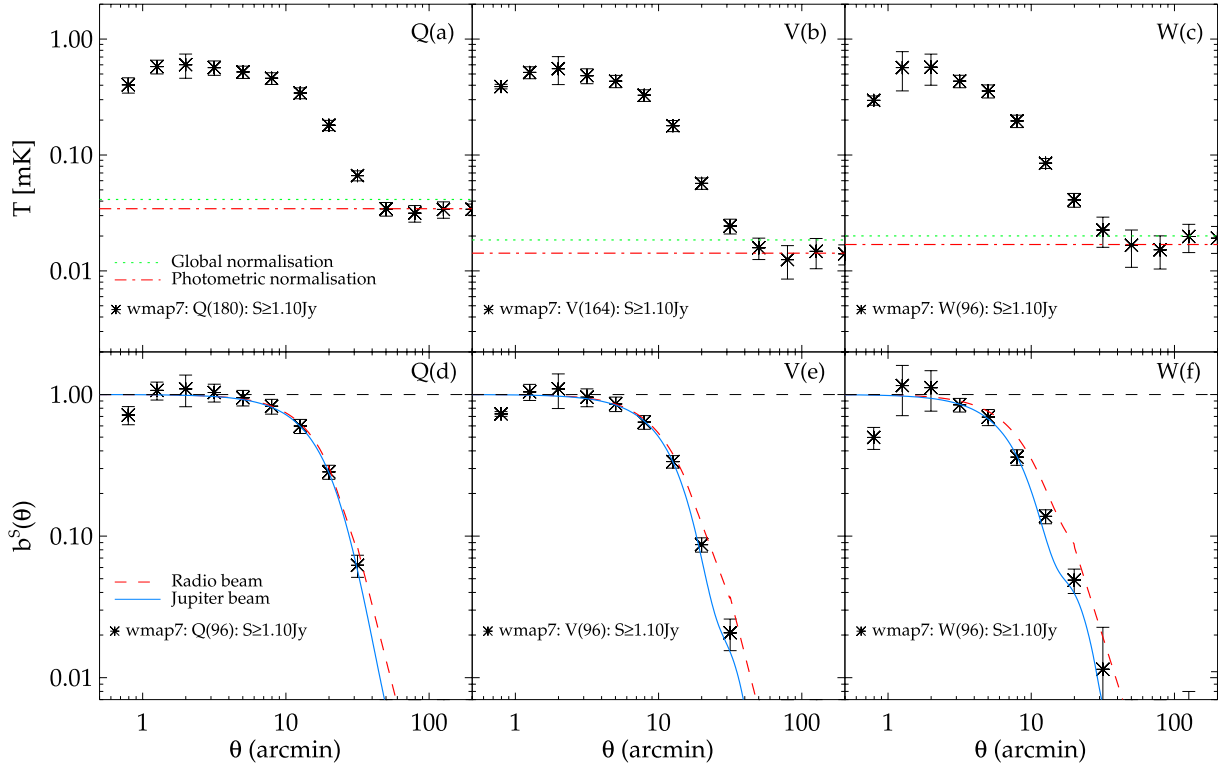


**Figure 4.** (a), (b), (c): the raw stacked *WMAP7* [*Q,V,W*] temperature profiles for the *WMAP7* sources of Gold et al. (2011) with the global mean and photometric background temperatures of the map plotted as dashed (green, red) lines. (d),(e),(f): the photometrically subtracted, stacked and re-normalized *WMAP7* [*Q,V,W*]  $b^s(\theta)$  profiles for the *WMAP7* sources of Gold et al. (2011). Also shown are the  $b^s(\theta)$  for the Jupiter beam (blue, solid) and the radio source fit (red, dashed) of Sawangwit & Shanks (2010a).

have used a flux limit of  $S \geq 1.1$  Jy. In Section 7.1, we shall check for the presence of Eddington bias in this particular data set using random simulations.

### 6.3 *WMAP7*-CMB-free radio sources

In the ‘CMB-free’ method (Chen & Wright 2009), *WMAP* sources are selected using the *Q,V,W* bands simultaneously to form an internal linear combination map with weights chosen to cancel out the CMB anisotropy signal. Again, any Eddington bias due to CMB fluctuations should be reduced in the case of this point-source catalogue. We therefore repeated our stacking analysis with the 417 *QVW* sources from the Gold et al. 2011 *WMAP7* ‘CMB-free’ catalogue – see Fig. 5. Overall we again see wider-than-expected profiles at *W*, broadly consistent with the results in Figs 3 and 4. Finally, we have also presented these results without the  $S \geq 1.1$  Jy flux limit, we note that the result is unchanged. This consistency is evidence for robustness of the result to Eddington bias.

### 6.4 NVSS radio sources

Point-source catalogues made at significantly lower frequencies than the *WMAP* bands are unlikely to be affected by Eddington bias due to CMB fluctuations, if identification is done independently of the *WMAP7* point-source catalogue. For example, point-sources selected at 1.4 GHz will have Rayleigh–Jeans temperature  $\approx 4500$  times higher than a source with similar flux density selected at *W* band ( $\approx 94$  GHz), i.e.  $T_{\text{RJ}} \propto \Omega_{\text{beam}}^{-1} \nu^{-2}$ , whereas the rms Rayleigh–Jeans temperature due to the CMB fluctuations stays roughly the same between the two frequency bands (Bennett et al.

2003). Therefore, we now stack co-added *WMAP7* temperature data centred around the positions of the 1147  $S_{1.4} > 1$  Jy NRAO VLA Sky Survey (NVSS) point sources. Fig. 6 shows the resulting *Q, V* and *W* profiles. We see that they are consistent with those measured using *WMAP5* total/bright sources in fig. 2 of Sawangwit & Shanks (2010a). However, the profiles do not appear as wide as the *WMAP5* faintest subsample despite the average flux of the NVSS sample at *WMAP* bands being  $\approx 3$  times lower.

Many of the NVSS sources are resolved into multiple components (Blake & Wall 2002). However, this is unlikely to cause the widening of the beam beyond  $\theta \gtrsim 6$  arcmin. Here, as a precautionary measure, we shall test the beam profile measured using the NVSS by excluding any source that has neighbouring source(s) within  $1^\circ$ . This extra condition reduces the number of  $S_{1.4} > 1.0$  Jy sources outside the *WMAP7* ‘point-source catalogue’ mask to 963. The resulting co-added beam profiles are also shown in Fig. 6. We see that the beam profiles are in good agreement with the previous results.

## 7 *WMAP* AND NVSS SOURCE CATALOGUE SIMULATIONS

### 7.1 Description

We made 100 Monte Carlo simulations to check our method and the robustness of the results. These simulations are due to Sawangwit (2011) who made them in the context of his test of the *W1* beam in the *WMAP5* data set. Thus, they are conservative in terms of both the errors they imply and the test of Eddington bias they make in our new context of the averaged DA’s (*W1–W4* in the *W*-band

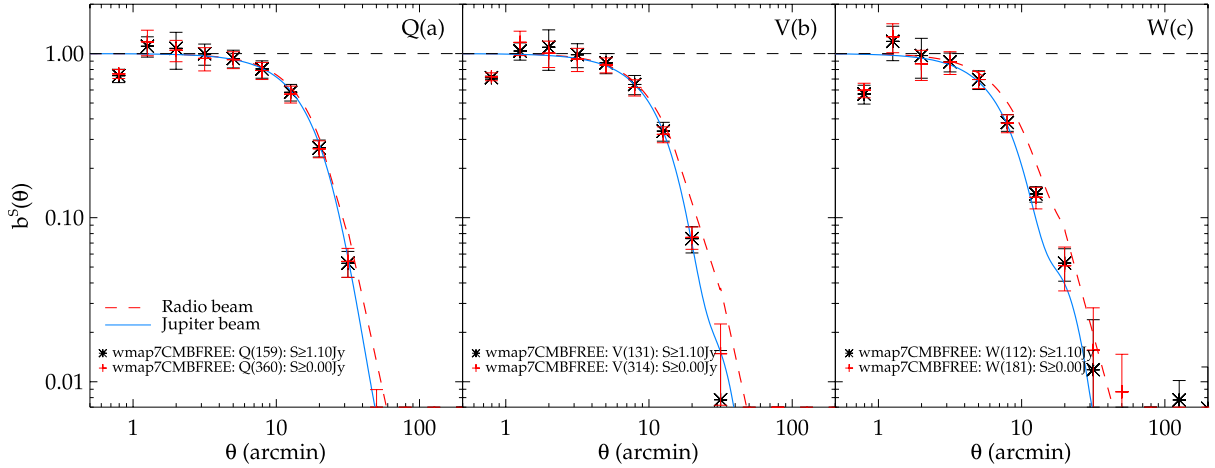


**Figure 5.** (a), (b), (c): the photometrically subtracted, stacked and re-normalized *WMAP7* [*Q,V,W*]  $b^s(\theta)$  profiles for the CMB-free *WMAP7* catalogues of Gold et al. (2011). Also shown are the  $b^s(\theta)$  for the Jupiter beam (blue, solid) and the radio source fit (red, dashed) of Sawangwit & Shanks (2010a). Any sensitivity to Eddington bias is shown in the profiles without the flux limit of  $S \geq 1.1$  Jy (lighter red, cross).

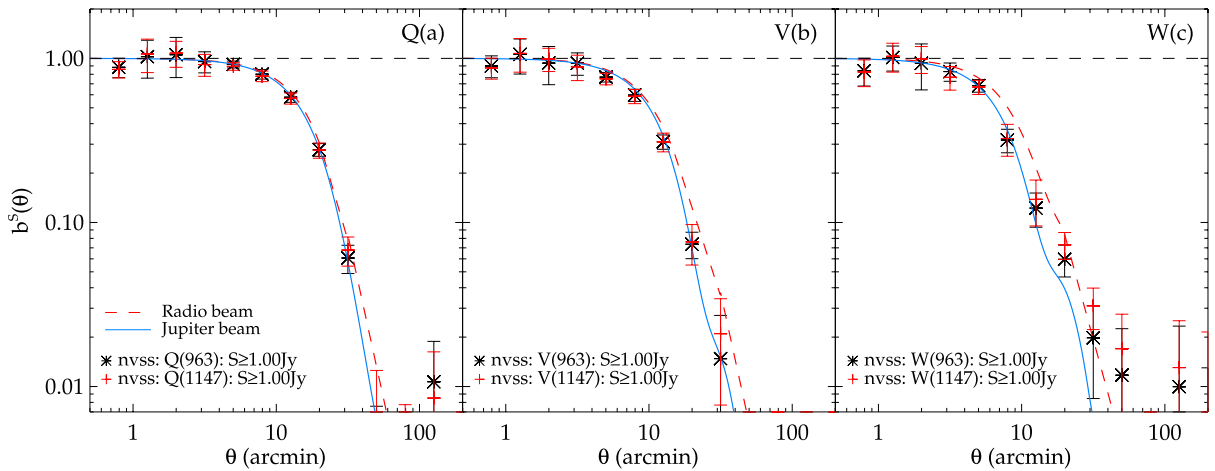


**Figure 6.** (a), (b), (c): the photometrically subtracted stacked *WMAP7* [*Q,V,W*]  $b^s(\theta)$  profiles for the NVSS sources. Also shown are the  $b^s(\theta)$  for the Jupiter beam (blue, solid) and the radio source fit (red, dashed) of Sawangwit & Shanks (2010a). Any sensitivity to close-pairs is shown in the profiles where sources with a neighbour within  $< 1^\circ$  have been excluded (lighter red, cross).

case) and the *WMAP7* data set. We followed the procedures described by Wright et al. (2009) – see also Chen & Wright (2009). For each set of simulations,  $\approx 10^6$  point sources are generated with a power-law distribution,  $N(> S) \propto S^{-1.7}$ , at *WMAP Q*-band (Bennett et al. 2003; Chen & Wright 2009). Their spectral indices,  $\alpha$ , are drawn from a Gaussian distribution with a mean  $-0.09$  and standard deviation  $0.176$  as characterized by the *WMAP5* point-source catalogue (Wright et al. 2009). The flux density for each object is scaled to the centre of the other four bands using the relation  $S_\nu \propto \nu^\alpha$ . The source positions are then randomly distributed on the sky and each source is assigned to a pixel in a HEALPIX  $N_{\text{side}} = 2048$  map. For a source with flux density  $S_\nu$ , the peak Rayleigh–Jeans temperature difference,  $\Delta T_{\text{RJ}}(0)$ , is given by equations (1) and (2), but with the  $\Omega_{\text{beam}}$  replaced by  $\Omega_{\text{pix}} = 2.5 \times 10^{-7}$  sr, solid angle of a  $N_{\text{side}} = 2048$  pixel. The publicly available *WMAP* maps (Section 2.2) are given in thermodynamic temperature (Limon et al. 2008). For a direct comparison with our results, we thus convert the simulated source’s  $\Delta T_{\text{RJ}}(0)$  to  $\Delta T_\ell(0)$  using equation (3).

Five temperature maps, one for each band, are then smoothed with the corresponding *WMAP* beam transfer function (Hill et al. 2009)

before being downgraded to  $N_{\text{side}} = 512$ . The simulated CMB temperature map (smoothed with an appropriate beam transfer function) constructed from *WMAP5* best-fitting  $C_\ell$  and pixel noise are then added to the source temperature maps. The pixel noise is modelled as a Gaussian distribution with zero mean and standard deviation  $\sigma = \sigma_0 / \sqrt{N_{\text{obs}}}$ , where  $N_{\text{obs}}$  is the number of observations in each pixel and  $\sigma_0$  is given for each DA and frequency band (Limon et al. 2008). Here, we use the *WMAP5*  $N_{\text{obs}}$  map to generate pixel noise for its corresponding band map.

## 7.2 Source detection

Next, we applied the five-band detection technique following procedures utilized by *WMAP* team (Bennett et al. 2003; Gold et al. 2011). First, the temperature maps are weighted by the number of observations in each pixel,  $N_{\text{obs}}^{1/2}$ . The weighted map is then filtered in harmonic space by  $b_\ell / (b_\ell^2 C_\ell^{\text{CMB}} + C_\ell^{\text{noise}})$  (e.g. Tegmark & de Oliveira-Costa 1998; Refregier, Spergel & Herbig 2000), where  $C_\ell^{\text{CMB}}$  is the CMB power spectrum and  $C_\ell^{\text{noise}}$  is the noise power, and  $b_\ell$  is the beam transfer function (Hill et al. 2009). The filter is

designed to suppress fluctuations due to the CMB at large scales and pixel noise at scales smaller than the beam width. We used the *WMAP5* best-fitting  $C_\ell$  for  $C_\ell^{\text{CMB}}$ . The  $C_\ell^{\text{noise}}$  are determined from pixel noise maps constructed using  $\sigma_0$  and five-year  $N_{\text{obs}}$  for each band as described above. We then search the filtered maps for peaks which are  $>5\sigma$ . Peaks detected in any band are fitted to a Gaussian profile plus a planar baseline in the unfiltered maps for all other bands. The recovered source positions are set to the best-fitting Gaussian centres in *W* band. The best-fitting Gaussian amplitude is converted to Rayleigh–Jeans temperature, using the relation given in equation (3), and then to a flux density using conversion factors,  $\Gamma^{\text{ff}}(\nu)$ , given in table 4 of Hill et al. (2009). In any given band, we only use sources that are  $>2\sigma$  and the fitted source width smaller than two times the beamwidth, following the *WMAP* team. The number of detected sources from 100 realizations are consistent with *WMAP5* point-source analyses by Wright et al. (2009) and Chen & Wright (2009). Our simulations also recover the input power-law  $N(>S)$  distribution down to the expected *WMAP5* limit,  $S \approx 1$  Jy, remarkably well – see Sawangwit (2011).

### 7.3 *WMAP* simulation results

For each simulation, we applied our beam profile analysis outlined in Section 4 (including a flux cut of  $S > 1.1$  Jy). The average beam profiles derived from 100 simulations are plotted in Figs 7(a)–(c), where the error bar represents their standard deviation in each angular bin. We found that even profiles as narrow as the *W1*-band Jupiter profile can be retrieved remarkably well out to 30 arcmin. The estimated uncertainties using these Monte Carlo simulations are consistent with the jack-knife error estimations. Note that the Monte Carlo error converges after  $\approx 60$ –70 simulations. The Monte Carlo simulations we performed here suggests that our method for

recovering beam profile by stacking temperature maps around point sources is robust and the jack-knife error estimation is reliable.

### 7.4 NVSS simulation results

Although we argued above that sources (i.e. their identifications and positions) selected at NVSS frequency are robust against the CMB fluctuations compared to *WMAP* bands, our beam analysis is still carried out using *WMAP* temperature maps. As we noted, the average flux of the  $S_{1.4} > 1$  Jy NVSS sources in the *WMAP* bands is approximately three times lower than the *WMAP* sample. Therefore, it is important to check whether the *WMAP* beam profiles can be robustly recovered using these NVSS sources. Again the results come from Sawangwit (2011) and were only applied to the *W1* detector assembly and use *WMAP5* data.

We again created 100 Monte Carlo simulations similar to those described above but without the five-band detection procedure since these sources are pre-detected by NVSS with high positional accuracy ( $\lesssim 1$  arcsec, Condon et al. 1998). The 963 NVSS source positions are used and fluxes at 1.4 GHz are extrapolated to *WMAP* *Q*, *V* and *W* bands assuming a mean spectral index,  $\alpha$ , of  $-0.45$  in order to mimic the average flux density observed in these bands. The temperature maps are smoothed with the corresponding *WMAP* (Jupiter) beam profiles. The simulated CMB fluctuations and radiometer noise are then added to the source temperature maps as described above. For each *WMAP* band, we applied our beam profile analysis to each of the 100 simulated maps (including a flux cut of  $S_{1.4} > 1$  Jy). The results are shown in Figs 7(d)–(f). The plot shows that with these NVSS radio sources, the *WMAP* beam profiles can be robustly recovered out to 30 arcmin and are not affected by the source clustering consistent with the semi-empirical calculation presented in Sawangwit & Shanks (2010a). We then take the standard deviation of the 100 simulated results in each angular bin as the  $1\sigma$  error.

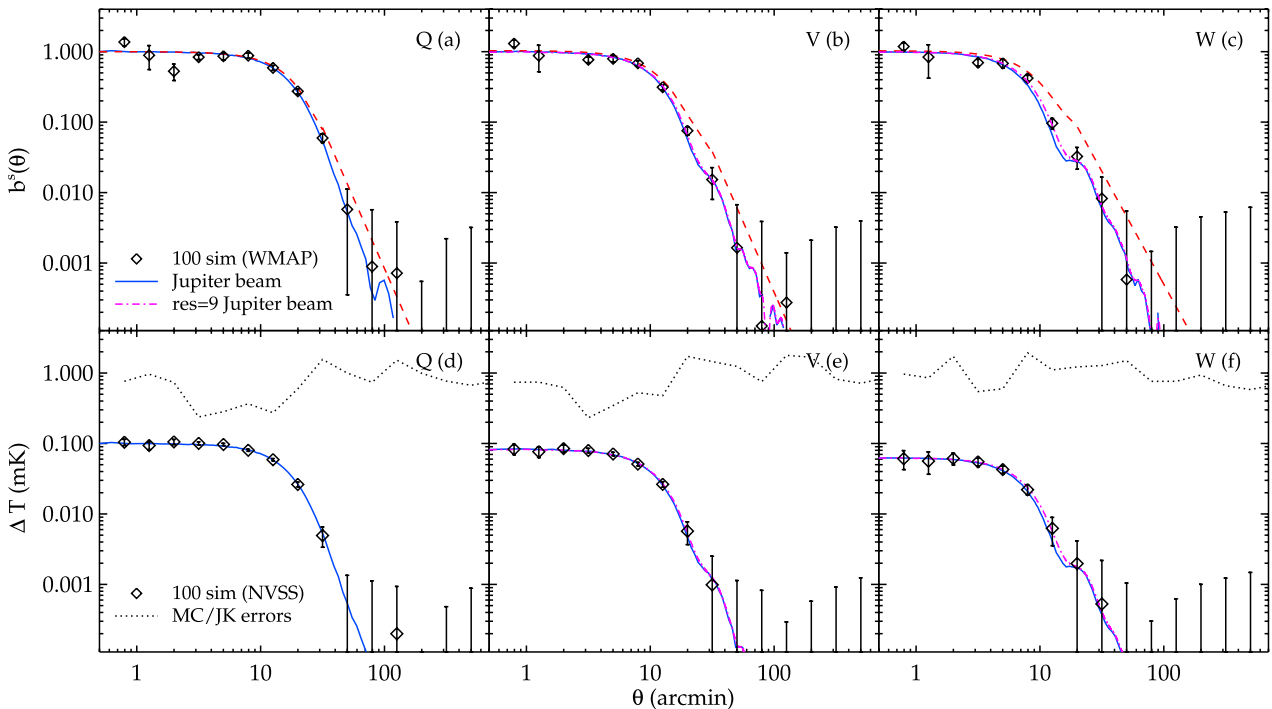


**Figure 7.** (a),(b),(c): the recovered [*Q1*,*V1*,*W1*] beam profiles using simulated *WMAP* point sources. The error bars are  $1\sigma$  rms of 100 simulations. The effect of pixelization on the profile measurement is shown by the magenta dot–dashed lines. (d),(e),(f): similar to (a–c) but now using  $S_{1.4} > 1$  Jy NVSS sources and without the re-normalization. The ratios between Monte Carlo and jack-knife errors are shown as the dotted lines.

The ratio of the Monte Carlo error to the jack-knife error is shown as the dotted line in Figs 7(d)–(f). The Monte Carlo and jack-knife errors are in good agreement except at scales  $< 10$  arcmin, where jack-knife errors are somewhat overestimates in  $Q$  and  $V$  bands.

The simulations suggest that when flux limited at  $S \geq 1.1$  Jy, the *WMAP*-selected source profiles are unaffected by Eddington bias. The simulations also support the accuracy of our empirical errors. The simulations suggest that the same conclusions apply when dealing with flux-limited ( $S_{1.4} > 1$  Jy) NVSS data.

## 8 POSSIBLE EXPLANATIONS OF WIDE RADIO SOURCE PROFILES

We now briefly consider possible explanations for the radio source profiles we have observed. We start by accepting that in the *WMAP7* data the profiles are less wide than found in the *WMAP5* data discussed by Sawangwit & Shanks (2010a). We regard our best current result to come from comparison with the *Planck* radio sources where we have checked the sources against spatial extension at *Planck* resolution and also rejected any that are contaminated by the CMB. This sample still rejects the *W*-band Jupiter beam at  $\approx 2$ – $3\sigma$  significance at 12.6 – 19.9 arcmin, about the same as the rejection of the previous best-fitting model from Sawangwit & Shanks (2010a). Therefore, it is not outside the bounds of possibility that the previous result may be explained by a statistical fluctuation in the *WMAP5* data. However, at the suggestion of the referee, we have now evaluated the rejection significance of the Jupiter beam using the full covariance matrix from our simulations, fitting in the range  $4 \text{ arcmin} < \theta < 20 \text{ arcmin}$ . For the Jupiter beam in the 7 yr co-added maps, we find formal rejection significances from the  $\chi^2$  distribution of  $[1.5 \times 10^{-3}, 3 \times 10^{-2}, 1.5 \times 10^{-2}, 9 \times 10^{-2}]$  for *Planck*, *WMAP7*, *WMAP7*-CMB-free and NVSS, respectively. Although we note that the overlap between these samples means that these results cannot be simply combined, the *Planck* sample itself represents an  $\approx 3\sigma$  rejection of the Jupiter beam. The low significance of the NVSS result simply reflects the larger errors associated with this fainter sample.

It is therefore still worth considering whether a wider beam could be related to other possible *WMAP* data problems. The first of these is the possible disagreement in *WMAP* flux comparisons with ground-based and *Planck* data sets noted by Sawangwit & Shanks (2010a) and also in this paper. Certainly a non-linearity like we first fitted to Fig. 1 goes in the right direction to explain a flatter than expected profile. Indeed, if the addition of Cas A, Cyg A, Tau A, 3C274 and 3C58 does imply that *WMAP* fluxes are simply offset from *Planck* and ground-based fluxes, then flux comparisons would be consistent with the wide beam. A logarithmic intercept of  $\approx -0.1$  implies the *WMAP* flux is  $\approx 80$  per cent of the corresponding *Planck* flux. Equally, we find the *W*-band *WMAP* Jupiter beam solid angle is  $\approx 80$  per cent of the 25.6 ms timing offset-derived beam's  $\Omega_{\text{beam}}$ . This is in agreement with the expectation from equation (1) that at fixed temperatures (i.e. those provided in the *WMAP* maps)  $S_{\text{tot}} \propto \Omega_{\text{beam}}$ .

However, more data at brighter fluxes is needed to check if the *WMAP* flux is non-linear or simply offset with respect to other data sets. We note that Malik et al. (in preparation) have used the CMB dipole to look for non-linearity in the *WMAP* temperature scale and failed to find any evidence for such an effect.

The second possible explanation for the wider than expected radio source profiles focused on the possibility that there was a timing offset between the *WMAP* antenna pointing and temperature data, as proposed by Liu & Li (2011). As well as causing effects at large scale

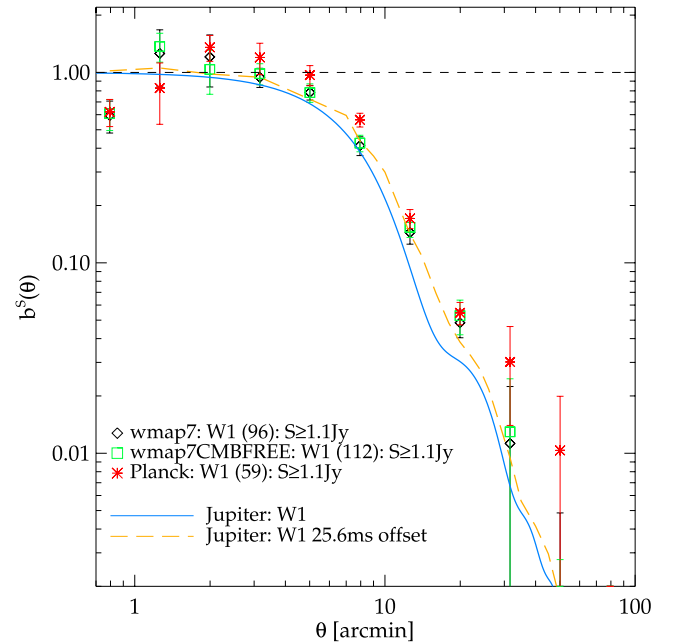


**Figure 8.** The photometrically subtracted, stacked and re-normalized *WMAP7* [ $Q1, V1, W1$ ]  $b^s(\theta)$  profiles for the *Planck*, *WMAP7* and CMB-free *WMAP7* catalogues. Also shown are the  $b^s(\theta)$  for the Jupiter beam (blue, solid) and a model showing the effect of a 25.6 ms timing offset on the *W1* Jupiter beam (orange, dashed) Sawangwit (2011).

due to a wrongly subtracted dipole, this scan pattern offset would cause a wider beam profile – see Moss, Scott & Sigurdson (2011). Sawangwit (2011) have calculated the beam pattern that a 25.6 ms timing offset would cause in the *W* band. The effect is approximately equivalent to a 3 arcmin Gaussian broadening of the beam. The calculation assumes the *W1* Jupiter beam and takes into account its initial asymmetry on the sky. After creating simulated *WMAP* time ordered data (TOD) that include point sources distributed in ecliptic latitude and then applying mapmaking to these data, Sawangwit (2011) found the azimuth-averaged beam profiles shown in Fig. 8 for both zero timing offset and the 25.6 ms timing offset with the latter giving a reasonable fit to the *Planck* data. More details are presented by Sawangwit (2011). These include further results based on using the dependence of beam shape with ecliptic latitude to try and determine the timing offset which marginally prefer zero timing offset. We note that Roukema (2010) made similar tests based on bright *WMAP* sources and found no evidence for a timing offset at the map-making stage. On the other hand, Liu & Li (2011) checked between offsets by minimizing dipole residuals and found strong evidence for a non-zero offset – see Sawangwit et al (in preparation). We note that the *WMAP* team have indicated that they use a timing offset of zero in which case the above agreement would simply represent a coincidence.

## 9 SZ RESULTS

### 9.1 *Planck* intermediate results

Our final aim is to make a comparison between the *Planck* ESZ and *WMAP* SZ results as described in Sections 3.2, 3.3 and 3.4. However, this involves reverse engineering the *Planck* SZ  $\Delta T(\theta)$  profiles. We therefore first use recently released *Planck* SZ data to check our reverse engineered *Planck* profiles. A series of

papers have been released as a follow up to the *Planck* ESZ data. Two papers in particular are relevant to corroborating the *Planck* profiles presented in this paper. In Planck Collaboration (2012b), the *Planck* Coma SZ profile has been published. Additionally, the ‘physical’ *Planck* SZ temperature profiles for the 62 local clusters in the Planck Collaboration (2011d) analysis have been published in Planck Collaboration (2012a). Below, we compare our reverse engineered profiles to these *Planck* data.

### 9.1.1 *Planck* Collaboration (2012b)

In Fig. 9, we now compare our *Planck* Coma SZ profiles to Planck Collaboration (2012b). We have shown two alternative *Planck* models in order to display the sensitivity of our results to the cluster size estimates. This is motivated by the significant difference between the value of  $R_{500} = 1.31$  Mpc used in Planck Collaboration (2012b) and the ESZ value,  $R_{500} = 1.13$  Mpc. Since the value for the integrated SZ signal,  $Y(5R_{500})$ , is degenerate with cluster size the ESZ value for  $Y(5R_{500})$  cannot be assumed. Therefore, in the first instance we do show an expected *Planck* temperature decrement using the ESZ values and calculated using equation (13). However, we also show a model which uses an alternative method for calculating the expected *Planck* profile. Here, the Planck Collaboration (2012b) value of  $R_{500}$  is used to calculate  $Y_{500}$  which can then be used to set the profile amplitude as shown in equation (A8). This method is solely dependent on the cluster size estimate, and is further described in Appendix A.

We find agreement between the Coma self-similar SZ model and the observed *Planck* temperature profiles. Although the *Planck* data does seem to have both a lower central amplitude and a slightly wider profile at large angular scales than the self-similar expectation. We note that corresponding differences between the self-similar model and the *Planck* data can be seen in the Planck Collaboration (2012b) analysis. A flatter inner profile may also be expected if any pixelization effects cause any further smoothing beyond the stated resolution of 10 arcmin. We also find reasonable agreement

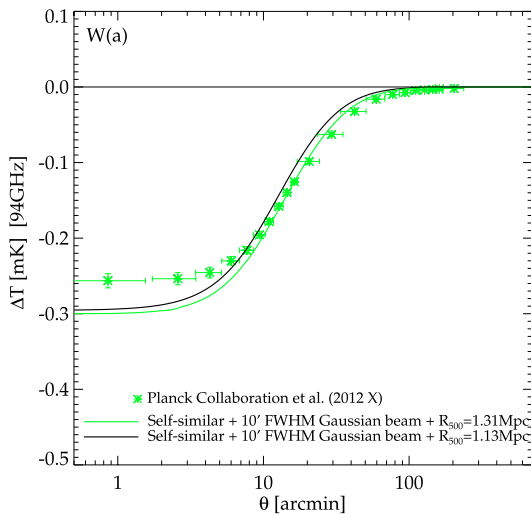


**Figure 9.** (a) The Planck Collaboration (2012b) *Planck* SZ decrement for the Coma cluster converted from RJ temperatures to a thermodynamic temperature at 94 GHz. Also shown are the *Planck* temperature decrements from equation (13) using the ESZ value of  $R_{500}$  (black, solid) and equation (A8) using the Planck Collaboration (2012b) value of  $R_{500}$  (green, solid). Both models are convolved with a 10 arcmin FWHM Gaussian beam appropriate to the Planck Collaboration (2012b) data.

between our two estimates of the *Planck* profile that use different cluster size estimates. Although, as expected, the model using the Planck Collaboration (2012b) value of  $R_{500}$  does provide a better fit to the *Planck* data. We conclude that the agreement between our *Planck* expectation and the underlying *Planck* profile supports the validity of our inversion of the *Planck* ESZ data to obtain *Planck* temperature profiles.

### 9.1.2 *Planck* Collaboration (2012a)

In Fig. 10, we compare our *Planck* ‘physical’ SZ profiles for the 62 Planck Collaboration (2011d) clusters to the ‘physical’ *Planck* profiles presented in Planck Collaboration (2012a). As was previously shown in Planck Collaboration (2012a), the *Planck* [100,70,44] GHz profiles are in agreement with the self-similar expectation. We now expand on this by attempting to use these results to verify our method of inverting the *Planck* ERCSC data to obtain *Planck* temperature profiles.

Since we again find that the Planck Collaboration (2011d) estimates of cluster size can be significantly different from the ESZ estimates we have used an alternative method of obtaining expected *Planck* temperature profiles. This method replicates Planck Collaboration (2012a)’s approach in assuming the Arnaud et al. (2010) self-similar model for the cluster and directly evaluating the Compton  $y$  parameter, as outlined in Appendix A. We have further followed Planck Collaboration (2012a)’s Section. 4.3 in using the Planck Collaboration (2011d) estimates of  $\theta_{500}$  and calibrate the central GFWF pressure,  $P_0$ , using the X-ray equivalent of the integrated SZ signal,  $Y_X$ .

As shown in Fig. 10 the two self-similar models convolved with 10 arcmin FWHM Gaussian beam profiles are in agreement beyond  $R_{500}$ . However, the inner profile of Planck Collaboration (2012a)’s model (black, solid  $\pm$  dotted) is substantially sharper than our model (green, solid). Although our model lies within the Planck Collaboration (2012a)’s  $\approx 1\sigma$  dispersion, we are comparing the stacked models (i.e. the statistical average) so the error range is a  $\sqrt{N} \approx 8$  smaller. We believe this difference is caused by the different stacking procedure used in Planck Collaboration (2012a), where depending on the noise properties within the bin either logarithmic or linear weightings were used. We have found that using these alternative weightings can accentuate the central peak of the profile, although not to the extent necessary for full agreement with Planck Collaboration (2012a). We currently do not have a full explanation for the difference in central amplitude.

## 9.2 *WMAP–Planck* ESZ comparison

We next show the stacked *WMAP7* temperature profiles for 151 clusters listed in the *Planck* ESZ catalogue. We are using the ‘photometric’ approach to background subtraction, with an annulus from 60 to 120 arcmin being used in  $W$  (and scaled according to beamwidth in  $Q$  and  $V$ ). The final models are based on the statistical average of the clusters.

We see in Fig. 11 that the *WMAP* data is an excellent fit to the *Planck* expectation. The fit between the *Planck* data and the *WMAP* data is not only good in all three  $[W, V, Q]$  bands but at all angular scales. We have further quantified the SZ measurements using jack-knife and bootstrap techniques all of which support *WMAP–Planck* agreement; however, we acknowledge these techniques do not include covariance.

In Fig. 11, we have shown the *Planck* self-similar models convolved with the power-law beams from Sawangwit & Shanks

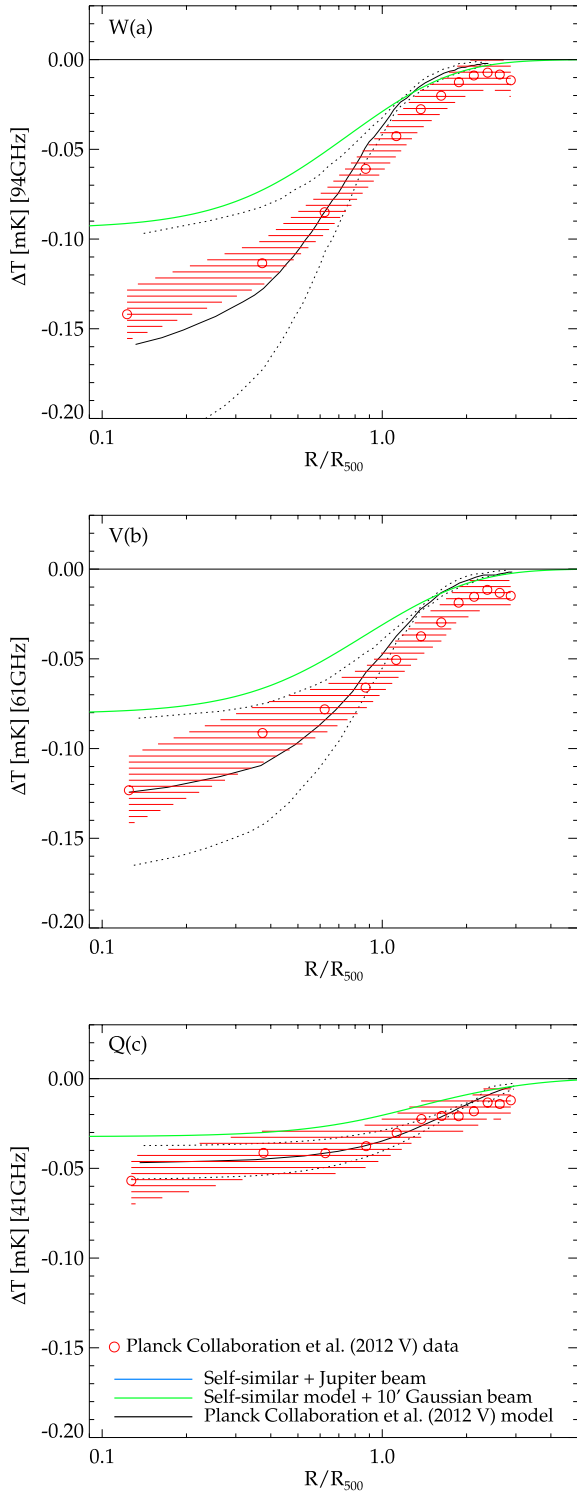


**Figure 10.** (a), (b), (c) The WMAP [W,V,Q] ‘physical’ SZ decrements for the 62 Planck Collaboration (2011d) clusters compared to the Planck temperature decrement from equation (13). The Planck profile is shown convolved with a 10 arcmin FWHM Gaussian (green, solid). We also show the 100 GHz Planck profiles presented in Planck Collaboration (2012a) converted into thermodynamic temperature at the WMAP band centre (red, stripes). The Planck Collaboration (2012a) models (black, solid) are plotted with their associated dispersions (black, dotted).

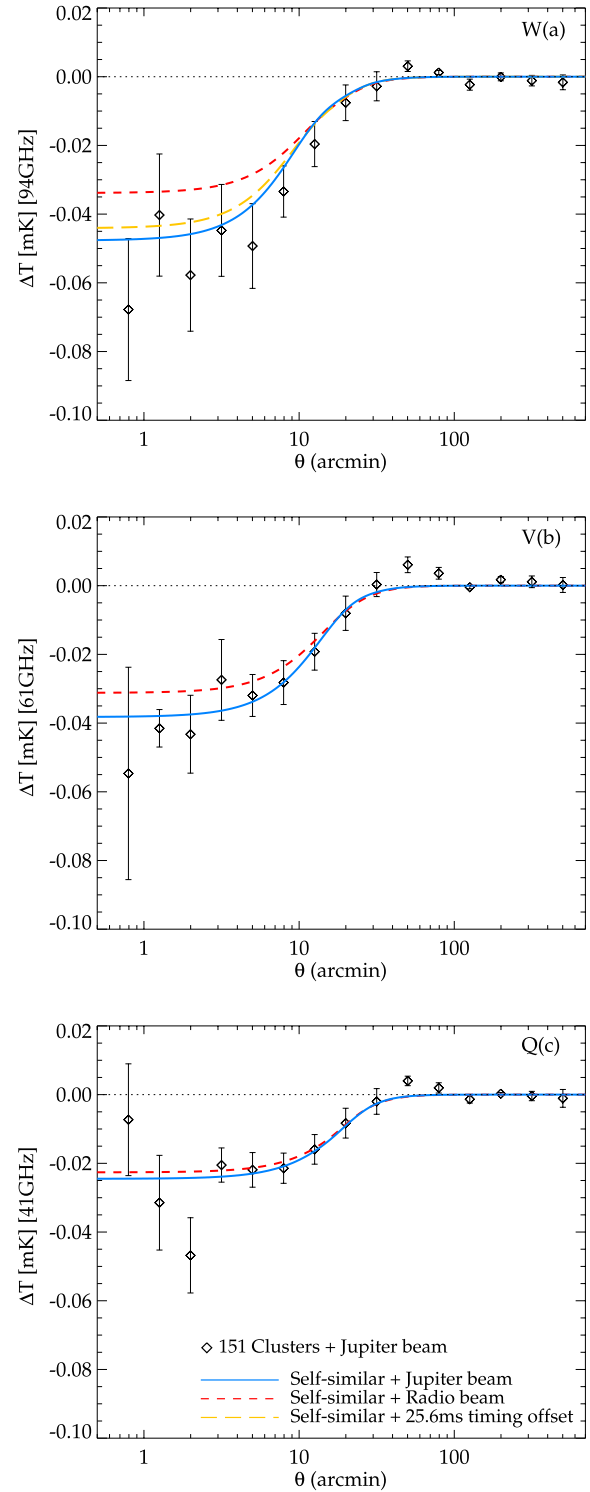


**Figure 11.** (a), (b), (c) The stacked WMAP [W,V,Q] SZ decrements for 151 Planck SZ clusters compared to the stacked Planck temperature decrement from equation (13). The Planck profile is shown convolved with a WMAP Jupiter beam, a beam fitted to the radio source profiles by Sawangwit & Shanks (2010a) and the Sawangwit (2011) timing offset derived beam.

(2010a). We find that in the case of the W band where the radio source profiles are most different from the Jupiter beam, there is now disagreement with the WMAP data with a deficit of  $\approx 20$  percent in the centre. In the Q and V bands, where the radio

source profiles are closer to the Jupiter beam, the wider beams give virtually no change in the agreement with the *WMAP* data. We conclude that the *Planck* SZ profiles disagree with the Sawangwit & Shanks (2010a) *WMAP5* radio source profile fits.

However, the Sawangwit (2011) timing offset derived beam, which provides an excellent fit to the radio source profiles as shown in Fig. 8, is significantly less wide than the Sawangwit & Shanks (2010a) beam. As shown in Fig. 11, we find that the timing offset beam only marginally reduces the central SZ temperature. We therefore conclude that the *WMAP* SZ results are not at sufficient S/N to differentiate between the timing offset derived and the Jupiter beams.

### 9.3 Coma

We have also looked at the *Planck* model fits for the Coma cluster and compared them to *WMAP*. Part of the motivation here is that previous authors, Lieu et al. (2006) and Bielby & Shanks (2007), have used Coma in investigating the consistency of the *WMAP* SZ signal with X-ray predictions.

In Fig. 12, we now show the *Planck* self-similar model for Coma (solid blue line) and see that it is substantially overestimated by the *WMAP* data. An analogous situation was found by Komatsu et al. (2011); in that the *WMAP* Coma *V*- and *W*-band profiles (potentially affected by CMB contamination) showed  $\mathcal{O}(100 \mu\text{K})$  more SZ signal than the optimal combined *V* and *W* profiles (free of CMB contamination).

Komatsu et al. (2011) proposed that Coma may sit on  $\mathcal{O}(100 \mu\text{K})$  downwards CMB fluctuation. Our results are entirely consistent with this interpretation because the *Planck* MMF method is essentially ‘CMB-free’ whereas our *WMAP* Coma data may still be contaminated by CMB fluctuations. On this basis, we also show in Fig. (12) a simple alteration to the *Planck* Coma SZ self-similar model by including a Gaussian with amplitude  $-100 \mu\text{K}$  and  $(\mu, \sigma) = (0 \text{ arcmin}, 60 \text{ arcmin})$  to mimic the effect of a downwards CMB contribution centred on Coma (blue, dashed). Agreement with the *WMAP* data is improved when a CMB contamination term is included. We therefore conclude that the difference between the *Planck* and *WMAP* Coma SZ profiles is the result of CMB contamination.

### 9.4 Bonamente et al. (2006) results

In Bielby & Shanks (2007), a *WMAP* discrepancy with the SZ/X-ray results of Bonamente et al. (2006) was presented. This is of particular interest as the Komatsu et al. (2011) *WMAP* SZ discrepancy was largely associated with the inner profile. The Bonamente et al. (2006) results complement this because they are weighted heavily to small scales because of the high resolution of their interferometric observations. In Fig. 13, we have therefore presented a stack of the 36 Bonamente et al. (2006) clusters that are unmasked in the *WMAP* temperature maps. We now find good agreement between the *WMAP* SZ decrements and the Bonamente et al. (2006) SZ/X-ray expectation. This is in contradiction to the results of Bielby & Shanks (2007). We have found this is attributable to Bielby & Shanks (2007)’s assumption that the cluster is well resolved with respect to the *WMAP* beam. As discussed in Section 3.4 this assumption introduces a systematic error into their 1D convolution with the *WMAP* beam profiles. We therefore now report no evidence for a *WMAP* SZ discrepancy with respect to the Bonamente et al. (2006) X-ray models.

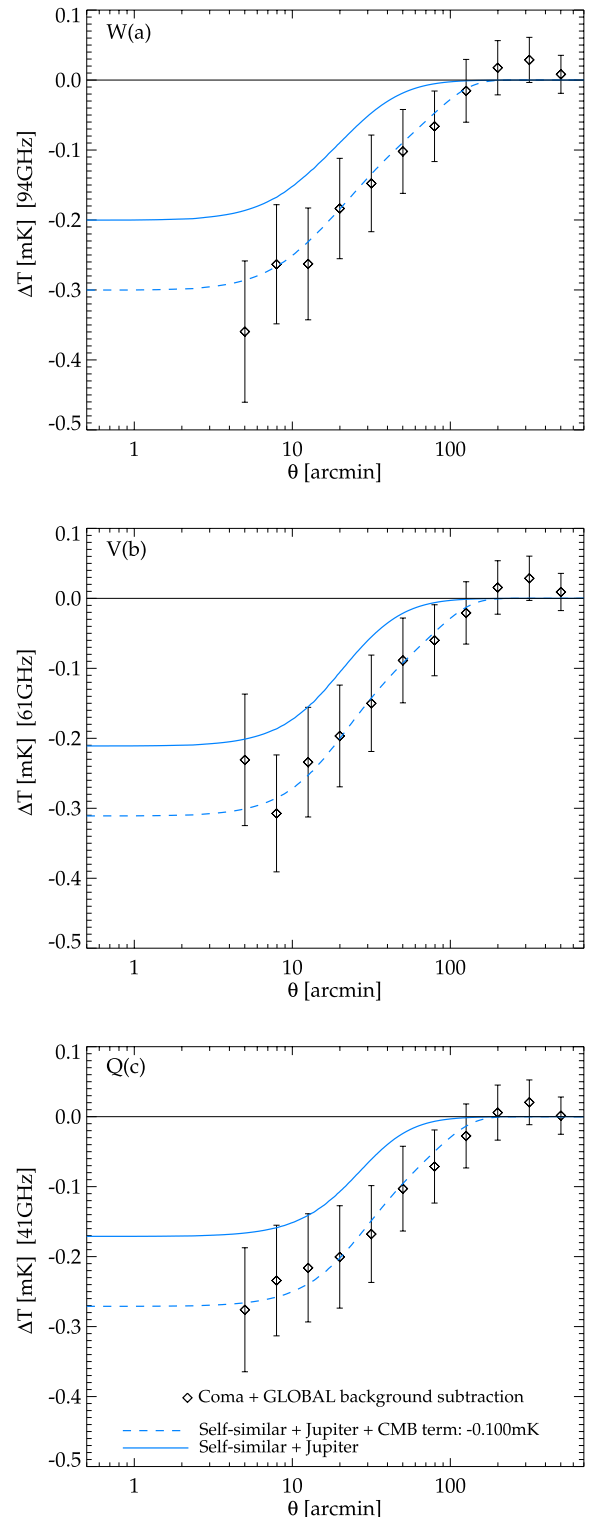


**Figure 12.** (a), (b), (c) The *WMAP* [W,V,Q] SZ decrements for the Coma cluster compared to the *Planck* temperature decrease from equation (13). The error within each annulus for this individual cluster is simply the standard deviation of the ESZ clusters and is therefore only indicative. The *Planck* profile is shown convolved with a *WMAP* Jupiter beam (blue, solid). We also show a model incorporating a  $100 \mu\text{K}$  downwards CMB fluctuation (blue, dashed).

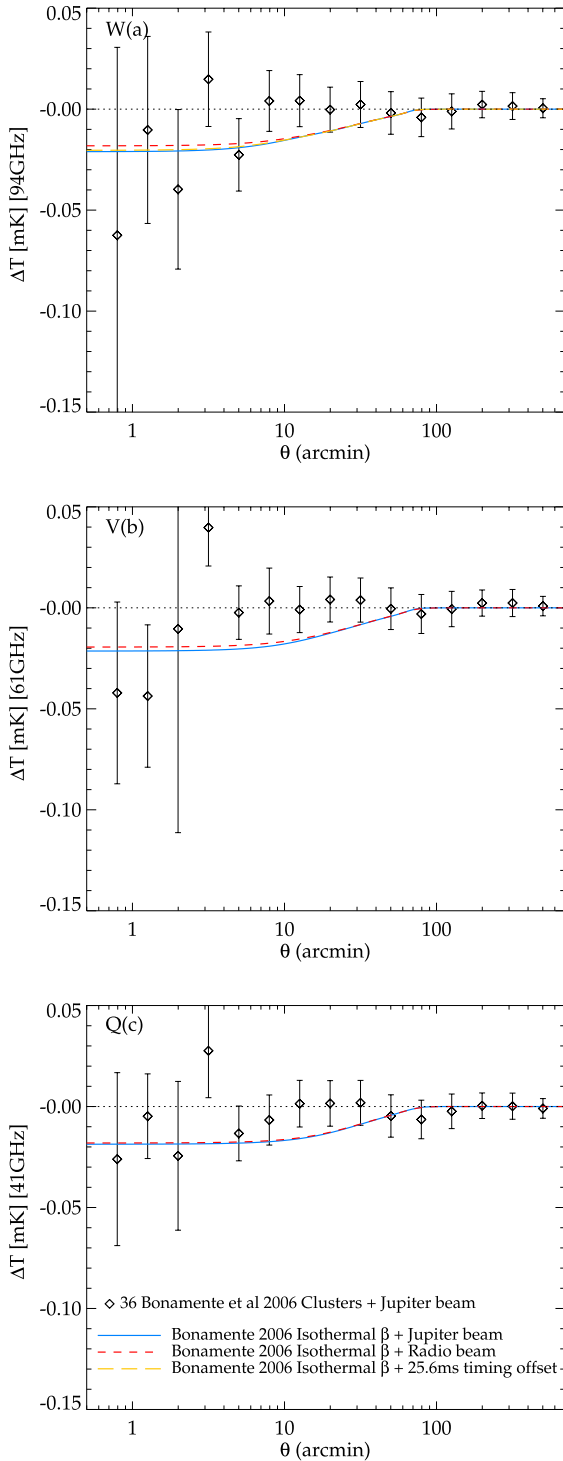


**Figure 13.** (a), (b), (c) The stacked WMAP [W,V,Q] SZ decrements for the 36 Bonamente et al. (2006) clusters that are unmasked in the WMAP temperature maps. This is compared to a stacked isothermal model based on the SZ/X-ray parameters fitted by Bonamente et al. (2006), convolved with the Jupiter beam, a beam fitted to the radio source profiles by Sawangwit & Shanks (2010a) and the Sawangwit (2011) timing offset derived beam.

## 10 DISCUSSION

The main criticism that was made of the previous results of Sawangwit & Shanks (2010a) was that the wide WMAP radio source profiles

may be caused by Eddington bias (Eddington 1913). Essentially, low S/N sources detected in the WMAP data may be contaminated by upwards CMB fluctuations and not balanced by downwards fluctuations. This could explain the wider than expected profiles, particularly at faint fluxes.

There may be some evidence for Eddington bias in the faintest WMAP5 W-band source sub-sample that was initially used by Sawangwit & Shanks (2010a). However, it was because of this the faintest sources were not used in Sawangwit & Shanks (2010a) fits of the beam profile and that a flux limit of  $S \geq 1.1$  Jy has been used in calculating our radio source profiles. We also note that the Planck sources show the wider beam independent of whether the CMBSUBTRACT flag applies. We further note that we have restricted the Planck sources to have an FWHM strictly less than the WMAP W-band beam profile width and find a wider than expected beam profile for these clear point sources. WMAP sources selected from a ‘CMB-free’ map and NVSS selected sources at low frequency also show the same wider than expected beam.

Furthermore, we have also run Monte Carlo re-simulations of the source detection, producing artificial source catalogues extracted from simulated CMB maps. Here, after applying the same cross-correlation technique as for the data, the WMAP beam was recovered as input (see Fig. 7), again arguing that these sources are little affected by Eddington bias.

The Planck data also confirms the non-linearity of WMAP fluxes, particularly in the W band, in the range previously used. Decreasingly non-linear effects are also seen at Q and V. But when ground-based and Planck data for the bright Weiland et al. (2011) sources are included in these comparisons, the evidence for non-linearity becomes less and it could still be that the discrepancy corresponds more to a constant offset.

Given that the beam profile widening is smaller in the WMAP7 data than in WMAP5, a scan pattern timing offset as discussed by Liu & Li (2011) becomes a more plausible explanation for this effect. We have seen that the effect, originally invoked as an explanation for the alignment of the low-order multipoles with the ecliptic, also provides a reasonable fit to the W-band beam profiles – see Fig. 8.

In our comparison of Planck–WMAP SZ decrements, we have found good agreement. Similarly, our WMAP SZ profile results are now in agreement with the X-ray data for the Bonamente et al. (2006) sample. This work is now in line with previous authors who when studying the integrated WMAP SZ signal  $Y_{\text{tot}}$  (as opposed to the Compton  $y$  parameter) have found no evidence for a WMAP discrepancy (Melin et al. 2011). We have no explanation for the Komatsu et al. (2011) WMAP SZ profile discrepancies at this point.

We have also found that our Planck profiles are consistent with the Planck results of Planck Collaboration (2012a) and Planck Collaboration (2012b). We interpret this as validating our method of inverting the Planck ERCSC data to obtain Planck SZ temperature profiles.

In response to a question from a referee, we note the Integrated Sachs–Wolfe (ISW) effect is at most a  $10 \mu\text{K}$  effect for clusters/superclusters (Granett, Neyrinck & Szapudi 2008). This is too marginal to affect the profiles we recover. The ISW is an even more negligible effect for radio sources, as observed by Nolta et al. (2004); Sawangwit et al. (2010), where it is shown to be  $\approx 0.3 \mu\text{K}$  effect. It is therefore highly unlikely to cause any bias to our results in either the SZ or radio source analyses.

We have also compared our results to those of Schultz & Huffenberger (2011) whose paper appeared while this one was being refereed. We compare our results directly to theirs in Fig. 14. The WMAP7 W3 graph they use as an example is significantly wider

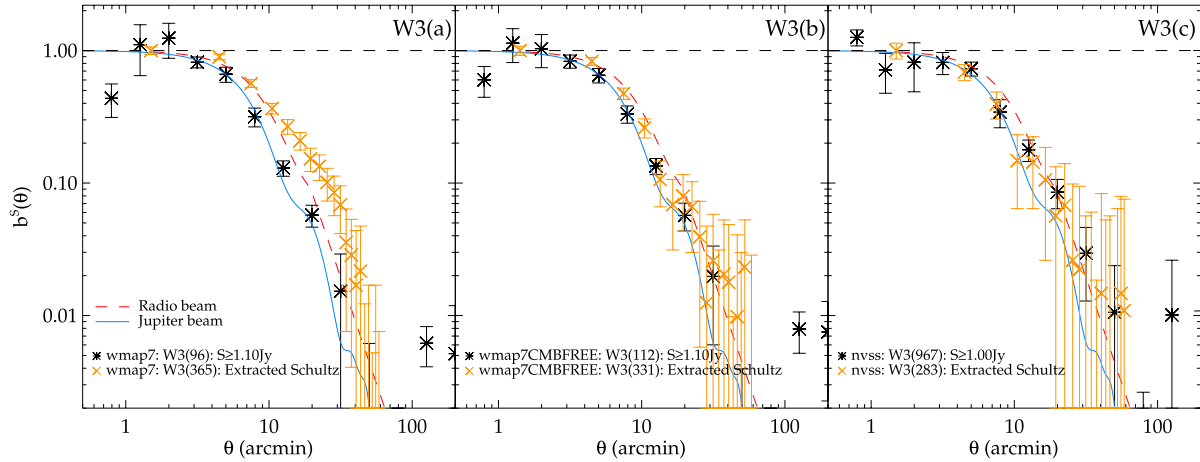


**Figure 14.** (a), (b), (c) The photometrically subtracted stacked *WMAP7* W3  $b^s(\theta)$  profiles for *WMAP7*, *WMAP7* CMB-free and NVSS catalogues as compared to the corresponding W3 results from Schultz & Huffenberger (2011) as taken from their fig. 5. Also shown are the  $b^s(\theta)$  for the Jupiter beam (blue, solid) and the radio source fit (red, dashed) of Sawangwit & Shanks (2010a).

than any profile shown by Sawangwit & Shanks (2010a) or here. This is because they have used a sample with no cut at all in terms of significance of detection or flux and clearly these data will be strongly affected by Eddington bias. We repeat that at the flux limits used here, the simulations show no sign of such bias and so we are confident that this criticism does not apply to our results. We note that there are additional quality cuts that Schultz & Huffenberger (2011) have made with respect to our work, such as an expanded mask and a culling of close pairs. However, we find that our results are unchanged when we apply them as well. We find that their *WMAP7*-CMB-free and NVSS beam profiles are very comparable to ours for the W3 band and they are wider than the Jupiter profile as can be seen. Schultz & Huffenberger (2011) suggest that the *WMAP7*-CMB-free profiles are wider due to errors on the radio source positions. However, their assumed positional errors may be overestimates for their stacked radio source profiles since the stacks are weighted towards the brighter radio sources which have more accurate positions. The fact that we are using 5 GHz GB6 and PMN positions accurate to sub-0.5 arcmin accuracy in the *WMAP* case and obtain *WMAP7*-CMB-free profiles consistent with Schultz & Huffenberger (2011) suggests that positional errors cannot be the explanation. The main difference with the NVSS results of Schultz & Huffenberger (2011) is their larger errors. Our NVSS sample is approximately four times larger than theirs due to our 1.4 GHz flux limit of 1 Jy compared to their 2 Jy limit, this (as well as our larger binning) explains most of the difference in errors. Otherwise the results appear entirely consistent.

We finally show in Fig. 15 the effect wide *Planck* radio source profiles (see Fig. 3 f) has on the *WMAP* W1/W2  $C_l$ . We take here the model with the 25.6 ms timing offset that gave a reasonable fit to the data in Fig. 8. Otherwise without the model, we would need to extrapolate a fit out to large angles. Then deconvolving the raw W1/W2  $C_l$  from PolSpice (Szapudi, Prunet & Colombi 2001) via equations 1 and 2 of Sawangwit & Shanks (2010a), we see that the  $C_l$  shows a modest increase in amplitude at  $\ell < 400$ , with a larger increase at  $\ell > 400$ . This reflects where the Jupiter and timing offset beam are different. At  $\ell < 400$ , there is very little difference between the Jupiter and the timing offset beam. We note that this region is essentially unconstrained by the radio source profiles. So the lack of change to the first acoustic peak is tied to the specific details of the timing offset model. A different model could give

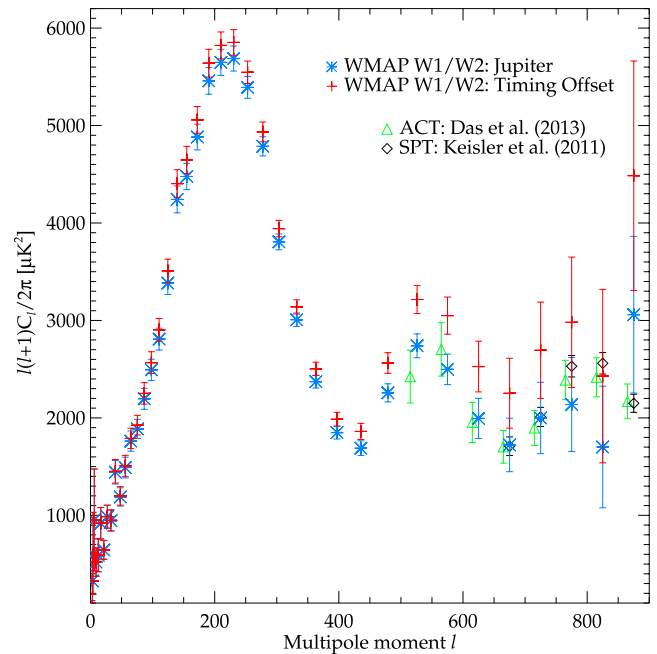


**Figure 15.** The *WMAP* W1/W2  $C_l$  result from deconvolving with the Jupiter beam (blue, stars) as compared to the result from deconvolving with the timing offset derived beam from Sawangwit (2011) and also shown in Fig. 8 (red, crosses).

significantly different results and therefore *WMAP7* first acoustic peak's amplitude and position relies heavily on the accuracy of the observed Jupiter beam beyond 30 arcmin scales, which is untested by our observations. However, it should be noted that although the timing-offset model reproduces the general form of the Silk damping tail, in detail there are significant differences at  $\ell > 500$  between this and the ground-based observations from South Pole Telescope (SPT; Keisler et al. 2011) and Atacama Cosmology Telescope (ACT; Sievers et al. 2013). We also note that it has been reported that there is agreement between *WMAP* and these ground-based observations (Hajian et al. 2011; Keisler et al. 2011). But the main point of Fig. 15 is simply to illustrate that such a beam profile can affect the CMB power spectrum.

## 11 CONCLUSIONS

We have investigated the beam profile of *WMAP* by comparing beam profiles from radio sources with the Jupiter beam profile. We have compared sources from *Planck*, *WMAP*, *WMAP* CMB-free and NVSS catalogues. We find that in all cases, the radio sources show wider profiles than the Jupiter beam with little indication of Eddington bias or dependence on the method of normalization. Applying our cross-correlation to realistic simulations strongly supports the accuracy of our beam profile measurements. However, it must be said that in the *WMAP7* data the *W* radio source profiles are less wide than previously found by Sawangwit & Shanks (2010a) in the *WMAP5* release. The rejection of the Jupiter beam is now only  $\approx 3\sigma$  in the *Planck* radio source comparison. But the rejection of the Jupiter beam is reasonably consistent between the admittedly overlapping radio source samples from *Planck*, *WMAP* and NVSS. We have therefore considered explanations for the wide profiles assuming that they are not statistical fluctuations. Two such possibilities are a non-linearity in the *WMAP* temperature scale and a timing offset in the *WMAP* scan pattern as discussed by Liu & Li (2011). The narrower profiles measured here compared to the Sawangwit & Shanks (2010a) *WMAP5* profiles increase the possibility of their being explained by a timing offset. However, we note that assuming a timing-offset derived beam results in a *WMAP* power spectrum which is in strong disagreement with independent ground-based observations from SPT and ACT.

We have also found discrepancies between *WMAP* fluxes compared to *Planck* and ground-based fluxes. For  $S < 30$  Jy the *WMAP* fluxes look to have a non-linear relation with *Planck* fluxes. However, when the further very bright sources discussed by Weiland et al. (2011) with ground-based and *Planck* measurements are included then this flux–flux discrepancy appears more like a linear than a non-linear offset.

We have compared stacked *WMAP* SZ decrements with those measured by *Planck* and by ground-based observations. In contrast to previous reports, we now find *WMAP* agrees with both the *Planck* and ground-based data. However, this work is not at high enough S/N to distinguish between the timing offset beam of Sawangwit (2011) and the *WMAP* Jupiter beam.

We have shown that transforming the Jupiter beam using a model that fits the radio source profiles results in small but significant changes to the *WMAP*  $C_\ell$ . At the least, a wider beam would imply a much larger uncertainty in the normalization and hence the estimate of  $\sigma_8$  from *WMAP*. Unfortunately, faint radio sources cannot check the *WMAP* beam at scales larger than 30 arcmin and a wider beam at these scales could, in principle, change the position, as well as the normalization, of even the first acoustic peak. Clearly it is important to continue to test the calibration and beam profile of *WMAP*, particularly in the *W* band. It will also be important to apply similar radio source beam profile checks to the recently released *Planck* maps and we shall report on this work elsewhere (Whitbourn 2013).

## ACKNOWLEDGEMENTS

JRW and TS acknowledge financial support from STFC (STFC grant no: ST/F007299/1). US acknowledges financial support from the Royal Thai Government. The observations in this paper are based on *Planck* (<http://www.esa.int/Planck>), an ESA science mission with instruments and contributions directly funded by ESA Member States, NASA and Canada.

We acknowledge the use of the Legacy Archive for Microwave Background Data Analysis (LAMBDA), part of the High Energy Astrophysics Science Archive Center (HEASARC). HEASARC/LAMBDA is a service of the Astrophysics Science Division at the NASA Goddard Space Flight Center. We also acknowledge the use of the TOPCAT utility, the NED archive and Ned Wrights Cosmology Calculator.

## REFERENCES

- Arnaud M., Pratt G. W., Piffaretti R., Böhringer H., Croston J. H., Pointecouteau E., 2010, *A&A*, 517, A92
- Aumont J. et al., 2010, *A&A*, 514, A70
- Bailey M. E., Sparks W. B., 1983, *MNRAS*, 204, 53p
- Bennett C. L. et al., 2003, *ApJS*, 148, 97
- Bennett C. L. et al., 2011, *ApJS*, 192, 17
- Bielby R. M., Shanks T., 2007, *MNRAS*, 382, 1196
- Blake C., Wall J., 2002, *MNRAS*, 337, 993
- Bonamente M., Joy M. K., LaRoque S. J., Carlstrom J. E., Reese E. D., Dawson K. S., 2006, *ApJ*, 647, 25
- Cavaliere A., Fusco-Femiano R., 1976, *A&A*, 49, 137
- Chen X., Wright E. L., 2009, *ApJ*, 694, 222
- Condon J. J., Cotton W. D., Greisen E. W., Yin Q. F., Perley R. A., Taylor G. B., Broderick J. J., 1998, *AJ*, 115, 1693
- Cotton W. D. et al., 2009, *ApJ*, 701, 1872
- Das S. et al., 2013, preprint (arXiv:1301.1037)
- Eddington A. S., 1913, *MNRAS*, 73, 359
- Gold B. et al., 2011, *ApJS*, 192, 15
- Granett B. R., Neyrinck M. C., Szapudi I., 2008, *ApJ*, 683, L99
- Gregory P. C., Scott W. K., Douglas K., Condon J. J., 1996, *ApJS*, 103, 427
- Griffith M. R., Wright A. E., 1993, *AJ*, 105, 1666
- Hajian A. et al., 2011, *ApJ*, 740, 86
- Hill R. S. et al., 2009, *ApJS*, 180, 246
- Hinshaw G. et al., 2003, *ApJS*, 148, 135
- Jarosik N. et al., 2003, *ApJS*, 145, 413
- Jarosik N. et al., 2011, *ApJS*, 192, 14
- Keisler R. et al., 2011, *ApJ*, 743, 28
- Kenney J. D., Dent W. A., 1985, *ApJ*, 298, 644
- Komatsu E. et al., 2011, *ApJS*, 192, 18
- Lieu R., Mittaz J. P. D., Zhang S.-N., 2006, *ApJ*, 648, 176
- Limon M. et al., 2008, Wilkinson Microwave Anisotropy Probe (*WMAP*): Seven-Year Explanatory Supplement, available at: <http://lambda.gsfc.nasa.gov/>
- Liszt H., Lucas R., 1999, *A&A*, 347, 258
- Liu H., Li T.-P., 2011, *ApJ*, 732, 125
- Lonsdale C. J., Doeleman S. S., Phillips R. B., 1998, *AJ*, 116, 8
- Macías-Pérez J. F., Mayet F., Aumont J., Désert F.-X., 2010, *ApJ*, 711, 417
- Melin J.-B., Bartlett J. G., Delabrouille J., 2006, *A&A*, 459, 341
- Melin J.-B., Bartlett J. G., Delabrouille J., Arnaud M., Piffaretti R., Pratt G. W., 2011, *A&A*, 525, A139
- Moss A., Scott D., Sigurdson K., 2011, *J. Cosmol. Astropart. Phys.*, 1, 1
- Mroczkowski T. et al., 2009, *ApJ*, 694, 1034
- Myers A. D., Shanks T., Outram P. J., Frith W. J., Wolfendale A. W., 2004, *MNRAS*, 347, L67
- Nagai D., Vikhlinin A., Kravtsov A. V., 2007, *ApJ*, 655, 98
- Nolta M. R. et al., 2004, *ApJ*, 608, 10
- Page L. et al., 2003, *ApJ*, 585, 566
- Page L. et al., 2003, *ApJS*, 148, 39
- Piffaretti R., Jetzer P., Kaastra J. S., Tamura T., 2005, *A&A*, 433, 101
- Planck Collaboration et al., 2011a, *A&A*, 536, A8
- Planck Collaboration et al., 2011b, Explanatory supplement [http://www.sciops.esa.int/SA/PLANCK/docs/ERCSC\\_Explanatory\\_Supplement.zip](http://www.sciops.esa.int/SA/PLANCK/docs/ERCSC_Explanatory_Supplement.zip)
- Planck Collaboration et al., 2011c, *A&A*, 536, A10
- Planck Collaboration et al., 2011d, *A&A*, 536, A11
- Planck Collaboration et al., 2012a, *A&A*, 550, A131
- Planck Collaboration et al., 2012b, *A&A*, 554, 140

- Pratt G. W., Böhringer H., Croston J. H., Arnaud M., Borgani S., Finoguenov A., Temple R. F., 2007, *A&A*, 461, 71
- Press W. H., Teukolsky S. A., Vetterling W. T., Flannery B. P., 1992, *Numerical Recipes*. Cambridge Univ. Press, Cambridge, p. 660
- Refregier A., Spergel D. N., Herbig T., 2000, *ApJ*, 531, 31
- Roukema B. F., 2010, *A&A*, 518, A34
- Sadler E. M., Ricci R., Ekers R. D., Sault R. J., Jackson C. A., de Zotti G., 2008, *MNRAS*, 385, 1656
- Salter C. J., Reynolds S. P., Hogg D. E., Payne J. M., Rhodes P. J., 1989, *ApJ*, 338, 171
- Sawangwit U., 2011, PhD thesis, Durham University
- Sawangwit U., Shanks T., 2010a, *MNRAS*, 407, L16
- Sawangwit U., Shanks T., 2010b, in Auge E., Dumarchez J., Tran Thanh Van J., eds, *Proc. 45th Rencontres de Moriond: Cosmology 2010, Lambda-CDM and the WMAP Power Spectrum Beam Profile Sensitivity*. GIOI, Vietnam, p. 53
- Sawangwit U., Shanks T., Cannon R. D., Croom S. M., Ross N. P., Wake D. A., 2010, *MNRAS*, 402, 2228
- Schultz K. W., Hufferberger K. M., 2011, *MNRAS*, 424, 3028
- Steppe H., Salter C. J., Chini R., Kreysa E., Brunswig W., Lobato Perez J., 1988, *A&AS*, 75, 317
- Sunyaev R. A., Zeldovich I. B., 1980, *ARA&A*, 18, 537
- Szapudi I., Prunet S., Colombi S., 2001, *ApJ*, 561, L11
- Tegmark M., de Oliveira-Costa A., 1998, *ApJ*, 500, L83
- Weiland J. L. et al., 2011, *ApJS*, 192, 19
- Whitbourn J. R., 2013, PhD thesis, Durham University
- Wright M., Birkinshaw M., 1984, *ApJ*, 281, 135
- Wright M. C. H., Sault R. J., 1993, *ApJ*, 402, 546
- Wright E. L. et al., 2009, *ApJS*, 180, 283

## APPENDIX A: SZ SELF-SIMILAR MODEL

In the self-similar SZ model as employed in the *Planck* ESZ, the fundamental parameters of a cluster are  $P_{500}$ ,  $M_{500}$  and  $R_{500}$ . Using the terminology of Arnaud et al. (2010),

$$M_{500} = \frac{4\pi}{3} R_{500}^3 500 \rho_{\text{crit}}, \quad (\text{A1})$$

$$R_{500} = D_a(z) \frac{\theta_{5R_{500}}}{5}. \quad (\text{A2})$$

A  $Y_{500}$  parameter corresponding to these is also defined,

$$Y_{500} = \frac{\sigma_t}{m_e c^2} \frac{4\pi R_{500}^3}{3} P_{500}, \quad (\text{A3})$$

which can be used as a characteristic SZ parameter instead of  $P_{500}$ . In equation (A3), the units of  $Y_{500}$  are  $\text{Mpc}^2$ , but are easily convertible to the  $\text{arcmin}^2$  units used in the ESZ and throughout this paper.<sup>5</sup>

<sup>5</sup>  $Y[\text{Mpc}^2] = \frac{1}{60^2} \left(\frac{\pi}{180}\right)^2 (D_a[\text{Mpc}])^2 Y[\text{arcmin}^2]$ .

This  $Y_{500}$  is a distinct quantity from  $Y(R_{500})$  as found by evaluating equation (9). The introduction of  $Y_{500}$  is well motivated because, as shown by Arnaud et al. (2010), it allows a scale-free description of equation (9)'s  $Y_{\text{sph}}$  and  $Y_{\text{cyl}}$  in terms of  $x = R/R_{500}$  as follows:

$$Y_{\text{sph}}(x) = Y_{500} I(x), \quad (\text{A4})$$

$$Y_{\text{cyl}}(x) = Y_{\text{sph}}(5R_{500}) - Y_{500} J(x), \quad (\text{A5})$$

where  $I(x)$  and  $J(x)$  are the spherical and cylindrical scaling functions,

$$I(x) = \int_0^x 3\mathcal{P}(u)u^2 du, \quad (\text{A6})$$

$$J(x) = \int_x^5 3\mathcal{P}(u)(u^2 - x^2)^{1/2} u du. \quad (\text{A7})$$

We therefore find that

$$Y_{\text{cyl}}(x) = Y_{500}(I(5) - J(x)). \quad (\text{A8})$$

Finally, we can use the above to calculate  $Y_{\text{cyl}}(R)$  and the Compton  $y$  parameter, where  $y(\theta) = \frac{d}{d\Omega} Y_{\text{cyl}}(\theta)$ . We now describe three methods for doing so.

(1) Using  $Y(5R_{500})$  as an amplitude. Since  $Y_{\text{cyl}}(5) = Y_{\text{sph}}(5) = I(5)Y_{500}$ , equation (A8) can be expressed as,

$$Y_{\text{cyl}}(R) = Y_{\text{cyl}}(5R_{500}) \left(1 - \frac{J(x)}{I(5)}\right). \quad (\text{A9})$$

This is the method we adopt in this paper, it is dependent on both  $Y(5R_{500})$  and  $\theta_{5R_{500}}$ .

(2) Using  $Y_{500}$  as an amplitude.  $Y_{500}$  can be calculated using  $M_{500}$  and  $P_{500}$ . We can therefore directly evaluate  $Y_{\text{cyl}}(R)$  using equation (A8). This method is independent of the *Planck* provided  $Y(5R_{500})$  and instead solely uses  $\theta_{5R_{500}}$ .

(3) Avoiding the integrated SZ signal. The Compton  $y$  parameter can be expressed as (Planck Collaboration 2012a),

$$y(r) = \frac{\sigma_t}{m_e c^2} \int_r^{R_{\text{tot}}} \frac{2P(r')r' dr'}{(r'^2 - r^2)^{1/2}}. \quad (\text{A10})$$

We can therefore directly evaluate the Compton  $y$  parameter if a self-similar cluster profile is assumed for  $P(r)$ . This method is independent of the *Planck* provided  $Y(5R_{500})$  and instead solely uses  $\theta_{5R_{500}}$ .

This paper has been typeset from a  $\text{T}_{\text{E}}\text{X}/\text{L}^{\text{A}}\text{T}_{\text{E}}\text{X}$  file prepared by the author.